BAMS Article

The Inner-Shelf Dynamics Experiment

Nirnimesh Kumar, James A. Lerczak, Tongtong Xu, Amy F. Waterhouse, Jim Thomson, Eric J. Terrill, Christy Swann, Sutara H. Suanda, Matthew S. Spydell, Pieter B. Smit, Alexandra Simpson, Roland Romeiser, Stephen D. Pierce, Tony de Paolo, André Palóczy, Annika O'Dea, Lisa Nyman, James N. Moum, Melissa Moulton, Andrew M. Moore, Arthur J. Miller, Ryan S. Mieras, Sophia T. Merrifield, Kendall Melville, Jacqueline M. McSweeney, Jamie MacMahan, Jennifer A. MacKinnon, Björn Lund, Emanuele Di Lorenzo, Luc Lenain, Michael Kovatch, Tim T. Janssen, Sean R. Haney, Merrick C. Haller, Kevin Haas, Derek J. Grimes, Hans C. Graber, Matt K. Gough, David A. Fertitta, Falk Feddersen, Christopher A. Edwards, William Crawford, John Colosi, C. Chris Chickadel, Sean Celona, Joseph Calantoni, Edward F. Braithwaite III, Johannes Becherer, John A. Barth, and Seongho Ahn

ABSTRACT: The inner shelf, the transition zone between the surfzone and the midshelf, is a dynamically complex region with the evolution of circulation and stratification driven by multiple physical processes. Cross-shelf exchange through the inner shelf has important implications for coastal water quality, ecological connectivity, and lateral movement of sediment and heat. The Inner-Shelf Dynamics Experiment (ISDE) was an intensive, coordinated, multi-institution field experiment from September–October 2017, conducted from the midshelf, through the inner shelf, and into the surfzone near Point Sal, California. Satellite, airborne, shore- and ship-based remote sensing, in-water moorings and ship-based sampling, and numerical ocean circulation models forced by winds, waves, and tides were used to investigate the dynamics governing the circulation and transport in the inner shelf and the role of coastline variability on regional circulation dynamics. Here, the following physical processes are highlighted: internal wave dynamics from the midshelf to the inner shelf; flow separation and eddy shedding off Point Sal; offshore ejection of surfzone waters from rip currents; and wind-driven subtidal circulation dynamics. The extensive dataset from ISDE allows for unprecedented investigations into the role of physical processes in creating spatial heterogeneity, and nonlinear interactions between various inner-shelf physical processes. Overall, the highly spatially and temporally resolved oceanographic measurements and numerical simulations of ISDE provide a central framework for studies exploring this complex and fascinating region of the ocean.

KEYWORDS: Ocean; Coastal flows; Internal waves; Mixing; Topographic effects; Waves, oceanic

https://doi.org/10.1175/BAMS-D-19-0281.1
Corresponding author: James Lerczak, jim.lerczak@oregonstate.edu
Supplemental material: https://doi.org/10.1175/BAMS-D-19-0281.2

In final form 12 November 2020

AFFILIATIONS: Kumar* and Fertitta—Department of Civil and Environmental Engineering, University of Washington, Seattle, Washington; **Lerczak, Pierce, Moum, McSweeney, Becherer,** and Barth**—College of Earth, Ocean, and Atmospheric Sciences, Oregon State University, Corvallis, Oregon; **Xu and Di Lorenzo**—School of Earth and Atmospheric Sciences, Georgia Institute of Technology, Atlanta, Georgia; **Waterhouse, Terrill, Spydell, de Paolo, Palóczy,** Miller, Merrifield, Melville,* MacKinnon, Lenain, Kovatch, Haney,* Grimes, Feddersen, and Celona**—Scripps Institution of Oceanography, University of California, San Diego, San Diego, California; **Thomson, Moulton,** and Chickadel**—Applied Physics Laboratory, University of Washington, Seattle, Washington; **Swann, Calantoni, and Braithwaite III**—Ocean Sciences Division, U.S. Naval Research Laboratory, Stennis Space Center, Mississippi; **Suanda****—Department of Marine Science, University of Otago, Dunedin, New Zealand; **Smit and Janssen**—Sofar Ocean Technologies, San Francisco, California; **Simpson, O'Dea, and Haller**—School of Civil and Construction Engineering, Oregon State University, Corvallis, Oregon; **Romeiser, Nyman, and Lund**—Rosenstiel School of Marine and Atmospheric Science, University of Miami, Miami, Florida; **Moore and Edwards**—Ocean Sciences Department, University of California, Santa Cruz, Santa Cruz, California; **Mieras****—National Research Council Research Associateship Program, Ocean Sciences Division, U.S. Naval Research Laboratory, Stennis Space Center, Mississippi; **MacMahan, Gough, and Colosi**—Department of Oceanography, Naval Postgraduate School, Monterey, California; **Haas**—School of Civil and Environmental Engineering, Georgia Institute of Technology, Atlanta, Georgia; **Graber**—Center for Southeastern Tropical Advanced Remote Sensing, University of Miami, Miami, Florida; **Crawford**—Naval Research Laboratory, Monterey, California; **Ahn**—Water Power Technologies, Sandia National Laboratories, Albuquerque, New Mexico

* Deceased

**** CURRENT AFFILIATIONS: Becherer**—Institute of Coastal Research, Helmholtz-Zentrum Geesthacht, Geesthacht, Germany; **Palóczy**—Department of Geosciences, University of Oslo, Oslo, Norway; **Moulton**—National Center for Atmospheric Research, Boulder, Colorado; **Mieras and Suanda**—Physics and Physical Oceanography Department, University of North Carolina, Wilmington, Wilmington, North Carolina;

The coastal ocean, from the shoreline to the mid–continental shelf with water depths ranging from 0 to about $O(100)$ m, spans regions with circulation patterns driven by distinct processes. Coastal ocean circulation regulates the transport of tracers like nutrients, pathogens, and pollutants critical to maintaining healthy ecosystems (e.g., Grant et al. 2005; Boehm et al. 2017), and controls lateral movement of heat, sediment, and entrained gases (e.g., Fewings and Lentz 2011; Sinnett and Feddersen 2019). Bottom sediment resuspension and the advection and mixing of particles, both organic and inorganic, contributes to variable optical clarity of coastal waters. Fluctuations in coastal ocean temperature modify the local stratification, sound speed, and shallow-water acoustics (e.g., Badiey et al. 2002).

Within the coastal ocean, the surfzone extends from the shoreline to the offshore extent of depth-limited wave breaking, while the midshelf region is categorized by nonoverlapping surface and bottom boundary layers separated by a distinct interior. The inner shelf (e.g., Lentz 1994; Lentz 1995b) is a transition region between the surfzone and the midshelf where the boundary layers can overlap. The dynamics within and immediately outside the inner shelf are complicated as surface waves, internal waves, wind, barotropic tidal processes, buoyancy, submesoscale eddies, and boundary layer–driven processes all contribute to changing the circulation pattern and local stratification on frictional, rotational, and longer time scales.

Previous studies targeting the inner shelf have well documented the wind-driven and surface gravity wave–driven dynamics on simple coastlines and bathymetry (e.g., Lentz and Fewings 2012), yet the role of complex, along-shelf-varying coastlines in modifying inner-shelf dynamics on subtidal and shorter time scales is not well understood. In addition, the importance of other physical mechanisms like the role of turbulence forced

by high-frequency processes (e.g., nonlinear internal waves) is both poorly understood and undersampled. Moreover, prior studies generally treated processes like subtidal wind-driven circulation in isolation from other inner-shelf physical processes. Nonlinear interactions between wind, surface gravity waves, internal waves, surface heat fluxes, turbulence, and rip currents are yet to be quantified.

Consequently, in order to understand and predict the exchange of water properties (heat, gases, sediment, pollutants, biota) across the inner shelf over a range of temporal and spatial scales the Office of Naval Research Inner-Shelf Dynamics Departmental Research Initiative coordinated field observations (in situ and remote sensing) and numerical modeling efforts on a 50-km section of coast off of central California, in the vicinity of Point Sal, California. Hereinafter, we refer to this experiment as the Inner-Shelf Dynamics Experiment (ISDE).

The principal goals of the ISDE are to (i) diagnose interactions between physical processes in the time-varying inner-shelf circulation, (ii) quantify the importance of along-coastline variability in creating complex circulation patterns on length scales of order 1–10 km, (iii) determine the role of turbulence in mixing tracer fluxes at subtidal and shorter time scales and in constraining momentum and energy transports on all time scales, and (iv) improve the predictive capability of numerical ocean and wave propagation models to simulate regional dynamics.

Here we report on the major findings and data products from the ISDE. A background describing the major physical processes in the inner shelf is considered in the second section. The field experiment and numerical model applications are considered in the third and fourth sections, respectively. Various important physical processes observed during the field experiment, complemented by numerical modeling efforts, are presented in the fifth section. In the sixth section we discuss the spatial heterogeneity of inner-shelf processes observed during the experiment, and the nonlinear interaction between multiple dynamical drivers of circulation and mixing. Findings from this work and suggested future directions for investigation are summarized in the last section.

Background

For decades, the inner shelf has been recognized as an important transition region between the mid–continental shelf and the surfzone. The inshore boundary of the inner shelf is generally agreed to be the surfzone (Garvine 2004; Lentz and Fewings 2012); however, the offshore extent and the dynamical definition of the inner shelf remain somewhat ambiguous and dependent on the dominant processes driving the circulation at a particular coastal region (Fig. 1). Mitchum and Clarke (1986) and Lentz (1994) define the inner shelf in the context of coastal wind-driven dynamics. In this context, the outer boundary of the inner shelf begins where the boundary layers overlap, causing a divergence and eventual shutdown in Ekman transport (Weisberg et al. 2001; Austin and Lentz 2002). Here, we briefly discuss the primary physical processes responsible for inner-shelf circulation and their role in cross-shelf material movement.

Seminal studies of the wind-driven inner shelf include those from the Coastal Ocean Dynamics Experiment (CODE; Beardsley and Lentz 1987; Lentz 1995a), west Florida continental shelf measurements (Weisberg et al. 2001, 2009), Coastal Ocean Processes Study (CoOP; Butman 1994), the Partnership for Interdisciplinary Studies of Coastal Oceans (PISCO; Kirincich et al. 2005), and from the Martha's Vineyard Coastal Observatory (Fewings et al. 2008). At subtidal time scales, these and other studies demonstrate the sensitivity of cross-shore transport to upwelling-favorable, downwelling-favorable, and cross-shore winds (Austin and Lentz 2002; Fewings and Lentz 2011; Horwitz and Lentz 2016), strength of stratification and structure of mixing (Lentz 1995b), alongshore pressure gradients (Lentz 1995b; Kirincich et al. 2013), and the presence of cross-shore buoyancy gradients

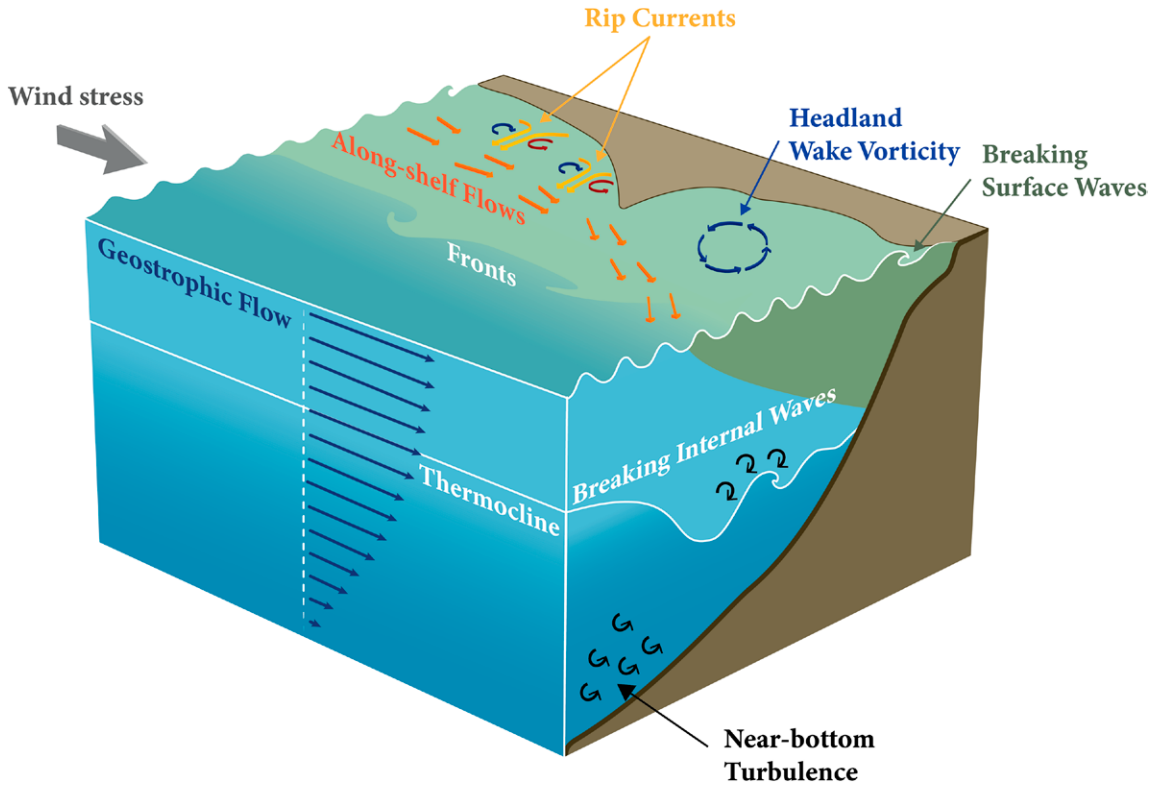

Fig. 1. Schematic of inner-shelf processes in the coastal ocean considered to be a part of the inner-shelf experiment. Surface waves propagating over the shelf become nonlinear and break generating circulation in the surfzone like rip currents, which eject onto the shelf. Wind and tidally driven along-shelf flows separate from the coastline and generate shelf eddies. Onshore-propagating internal waves also become nonlinear and lead to overturning and mixing in the water column. Additional mixing occurs at the bottom-boundary layer.

(Fewings et al. 2008; Horwitz and Lentz 2014). Previous studies have also demonstrated the role of Stokes drift by surface gravity waves outside the surfzone as a dominant mechanism for cross-shore transport (Lentz et al. 2008; Lentz and Fewings 2012), and radiation stress gradients as a potential leading-order term in the inner-shelf cross-shore momentum budget (Lentz et al. 1999; Fewings and Lentz 2010).

Internal waves are important to the inner shelf over a range of time and spatial scales. Highly nonlinear internal tides and high-frequency internal waves occur in the inner shelf and are responsible for large changes in stratification and strong cross-shore currents over short time scales (Lee 1961; Cairns 1967; Winant 1974; Scotti and Pineda 2004; Sinnett et al. 2018; McSweeney et al. 2020b; Feddersen et al. 2020), and also transport heat from the inner shelf to the surfzone (e.g., Sinnett and Feddersen 2019). These waves also transport plankton and nutrients across the inner shelf (Shanks and Wright 1987; Pineda 1991; Leichter et al. 1998; Lennert-Cody and Franks 1999; Shroyer et al. 2010) and can resuspend and transport sediment (Butman et al. 2006).

Turbulence and mixing generated by internal wave dissipation leads to vertical fluxes of tracers and material (Fig. 1; Bourgault et al. 2008; Walter et al. 2014; Woodson 2018), and enhance stresses which may augment surface and bottom boundary layer overlap (e.g., Palóczy et al. 2021). Processes on a daily time scale such as diurnal heating and diurnal winds can also change the inner-shelf currents and stratification (Lerczak et al. 2003; Cudaback and McPhee-Shaw 2009; Molina et al. 2014; Aristizábal et al. 2017; Walter et al. 2017; Feddersen et al. 2020). In addition, buoyancy-driven flows can dominate the inner-shelf circulation; for example, by river discharge (Allen et al. 1983; Mazzini et al. 2014) or a buoyant response

to changes in alongshore winds (Woodson et al. 2009; Washburn and McPhee-Shaw 2013; Suanda et al. 2016).

Mesoscale and submesoscale variability due to eddies, filaments, and fronts is often large on continental shelves and slopes and these are dominant mechanisms for exchange between the continental shelf and open ocean (Huyer and Kosro 1987; Barth 1994; Capet et al. 2008; Gula et al. 2016a). Recent observational and numerical studies have demonstrated the significance of submesoscale processes in causing variability in circulation and driving transport and dispersion in the inner shelf (Nidzieko and Largier 2013; Kirincich 2016; Kirincich and Lentz 2017; Dauhajre et al. 2019) and delivering nutrients to coastal ecosystems (Bassin et al. 2005).

Flow separation past abrupt bathymetry like headlands, capes, and coastal promontories leads to vorticity generation and complex three-dimensional circulation patterns (e.g., Fig. 1). Developed eddies can potentially pair, interact, or coalesce to form a wide variety of tidally rectified and residual flows (Signell and Geyer 1991; Pawlak and MacCready 2002; Callendar et al. 2011). The pressure anomalies associated with topographic eddy generation may play an order one role in the form drag that removes momentum from low-frequency alongshore flows (Warner et al. 2013). These eddies also control the dispersion of dissolved pollutants, floating organisms, and sediment (e.g., Pawlak et al. 2003; Doglioli et al. 2004; Roughan et al. 2005; Jones et al. 2006), enhance biological productivity and larval retention (Karnauskas et al. 2011; Gove et al. 2016), and influence local water-column mixing and dissipation (Canals et al. 2009; White and Helfrich 2013; Dewar et al. 2015; Gula et al. 2016b; MacKinnon et al. 2019).

Material movement also occurs between the shoreline and the inner shelf through the surfzone (Fig. 1). Rip currents and surfzone eddies are the primary known mechanism for cross-shore transport (e.g., MacMahan et al. 2006; Dalrymple et al. 2011; Castelle et al. 2016). Bathymetrically controlled rip currents result from wave breaking on alongshore-variable bathymetry and are typically strongest for shore-normal waves, larger wave height, and lower tidal elevation (Haller et al. 2002; MacMahan et al. 2010; Bruneau et al. 2011; Austin et al. 2013, 2014; Moulton et al. 2017). Stochastic surfzone eddy processes including wave-group vortices (e.g., Long and Özkan-Haller 2009), shear instability of alongshore currents (e.g., Özkan-Haller and Kirby 1999; Noyes et al. 2004), and transient rip currents resulting from short-crested wave breaking (e.g., Peregrine 1998; Spydell and Feddersen 2009; Clark et al. 2012; Feddersen 2014) are also known to be a major driver of cross-shore exchange. Infrared and X-band radar imaging of ejection events (e.g., Marmorino et al. 2013; Haller et al. 2014), dye releases (e.g., Hally-Rosendahl et al. 2014, 2015; Hally-Rosendahl and Feddersen 2016), and recent numerical modeling studies (e.g., Suanda and Feddersen 2015; Kumar and Feddersen 2017b; O'Dea et al. 2021) suggest that transient rip currents lead to cross-shore exchange up to several surfzone widths from the coastline.

The list of physical processes discussed here is not exhaustive as other processes may control the circulation and stratification in the inner shelf. The relative role of aforementioned physical processes has been previously considered (e.g., Fewings et al. 2008), yet additional investigation is required to further constrain the implications for exchange through the inner shelf, especially for locations with complex overlap of processes and variable along-shelf coastline and bathymetry.

Experiment description

The field component of ISDE brought together a novel and synergistic suite of measurement strategies, sensors, and platforms to study a heterogeneous coastal region from the outer shelf to the nearshore within the Santa Maria basin, off of central California, spanning

alongshore from south of Purisima Point to Pismo Beach and centered on Point Sal (Fig. 2 and Table 1; the offshore tip of Point Sal is located at 34.9030°N, 120.6721°W). Point Sal is a prominent 2-km-wide asymmetric headland, where the coast is rocky and the coastline bends approximately 120°. Bathymetry offshore off Point Sal is steep and rocky to ≈15 m depth, with several shoals and outcrops within 500 m. South from Point Sal, the rocky coastline extends eastward for 2.5 km before bending to the south where bathymetry contours are alongshore uniform and bottom slopes are less steep. To the north of Point Sal, offshore of Oceano, the shoreline is generally straight, and the offshore bathymetry is roughly alongshore uniform but with sandy crescentic bars close to shore. South of Oceano, a rocky outcrop extends several kilometers offshore at Mussel Point.

Following preliminary field measurements in 2015 to help define conditions and refine measurement strategy (Allen et al. 2018; Colosi et al. 2018), the main experiment took place from late August to early November 2017, and the field site covered about 50 km along the coast and 15 km across shore in water depths ranging from 5 to 150 m (Fig. 2). The field campaign included moored and bottom time series measurements, ship and small boat surveys, surface drifters, and remote sensing from land, airplanes, and space.

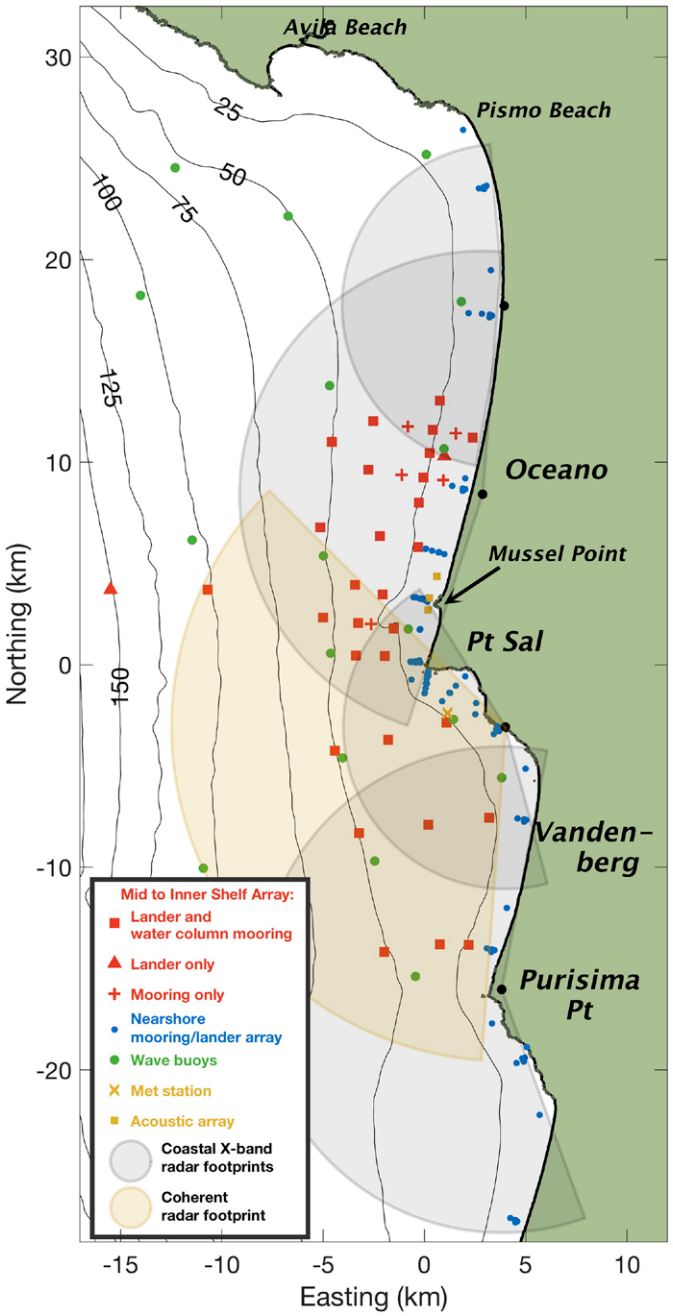

Fig. 2. Map of the Inner-Shelf Dynamics Experiment study site, showing locations of moorings and bottom landers and measurement footprints of coastal X-band and coherent radar systems. Contour lines represent water depth in meters.

Time series from moored and bottom-mounted sensors. A total of 173 moorings and bottom landers were deployed during the experiment to measure time series of temperature, salinity, current velocity, turbulence, surface gravity waves, and suspended sediment (Fig. 2). Water-column temperature and salinity were measured along vertical mooring lines at 95 locations. Temperature sensors spanned the water column with vertical spacing between sensors of 1–5 m at the deeper locations and 1 m or less in shallow water. Limited salinity measurements were also made. However, temperature was the dominant parameter controlling density, with salinity varying by less than 0.3 psu across the study site during the entire experiment consistent with previous studies (Washburn et al. 2011). Sensor sample intervals varied from 0.5 to 30 s (McSweeney et al. 2020b).

At 52 locations, moorings were paired with bottom landers, separated horizontally by about one water depth. Each lander was equipped with an upward-looking acoustic Doppler current profiler (ADCP) to measure current velocities. The vertical resolution was dependent

Table 1. Inner-Shelf Dynamics Experiment observational and modeling efforts, along with the names and affiliations of the principal investigators. Applied Physics Laboratory (APL), Georgia Tech University (GTA), Naval Postgraduate School (NPS), Naval Research Laboratory (NRL), Oregon State University (OSU), Scripps Institution of Oceanography (SIO), Sofar Ocean Technologies (Sofar), University of California Santa Cruz (UCSC), University of Miami (U Miami), University of Otago (UO), University of Washington (UW).

Shipboard surveys	
R/V *Oceanus*	J. Barth (OSU), J. Lerczak (OSU)
CTD towed surveys + ADCP	J. Barth (OSU)
Thermistor bowchain	J. MacKinnon (SIO), A. Waterhouse (SIO)
Shipboard radar	R. Romeiser (U Miami), H. Graber (U Miami)
Turbulence measurements	J. Moum (OSU)
Radiometer	C. Chickadel (APL)
Biosonics	J. Becherer (OSU)
R/V *Sally Ride*	J. Colosi (NPS), J. MacKinnon (SIO)
CTD towed surveys	J. MacKinnon (SIO), A. Waterhouse (SIO)
Thermistor bowchain	J. MacKinnon (SIO), A. Waterhouse (SIO)
Turbulence measurements	J. MacKinnon (SIO), A. Waterhouse (SIO), J. Moum (OSU)
Radiometer	C. Chickadel (APL)
R/V *Sproul*	A. Palóczy (SIO)
Flowthrough data	A. Palóczy (SIO)
CTD casts + ADCP	A. Palóczy (SIO)
Thermistor bowchain	A. Palóczy (SIO)
R/V *Kalipi*	J. Lerczak (OSU)
CTD casts + ADCP	J. Lerczak (OSU)
R/V *Sally Ann*	F. Feddersen (SIO)
CTD casts + ADCP	F. Feddersen (SIO)
R/V *Sounder*	J. Thomson (APL)
CTD casts + ADCP	J. Thomson (APL)
Fluorometer	M. Moulton (APL)
In situ	
Moorings	J. Lerczak (OSU), J. Barth (OSU), J. MacKinnon (SIO), A. Waterhouse (SIO), J. Colosi (NPS), J. Calantoni (NRL), F. Feddersen (SIO), J. MacMahan (NPS)
Spotter drifters	P. Smit (Sofar)
Surface drifters	F. Feddersen (SIO)
SWIFT drifters	J. Thomson (APL)
Wave buoys	E. Terrill (SIO)
Bottom pressure	J. Moum (OSU)
Meteorological measurements	
Land-based MET stations	J. Thomson (APL), M. Haller (OSU)
MET buoy data	E. Terrill (SIO)
Remote sensing	
Land-based radar	M. Haller (OSU), E. Terrill (SIO)
Aircraft No. 1: Modular Aerial Sensing System (MASS; topographic lidar; sea surface temperature; visible, Interferometric SAR, infrared, and hyperspectral imagery)	L. Lenain (SIO)
Aircraft No. 2: Compact Airborne System for Imaging the Environment (CASIE; visible and thermal infrared imaging, radiometer, along-track interferometric C-band SAR)	C. Chickadel (APL), M. Moulton (APL)
Drone imagery	M. Haller (OSU)
Satellite SAR	R. Romeiser (U Miami), H. Graber (U Miami)
Numerical modeling	
Nested applications	N. Kumar (UW), S. Suanda (UO), A. Miller (SIO)
Forecasts and sensitivity	A. Miller (SIO), E. DiLorenzo (GTA), K. Haas (GTA)
Data assimilation	C. Edwards (UCSC), A. Moore (UCSC)

on instrument frequency and water depth, but ranged between 0.25 and 3 m. Ping averaging resulted in temporal intervals of 0.5 to 30 s, and some of the ADCPs were five-beam instruments with sample frequencies of 1, 2, or 8 Hz allowing for the measurement of currents of surface gravity waves and calculations of turbulent stresses. Most landers were also equipped with temperature sensors, programmed to sample at the same rate as the mooring sensors. In addition, high-precision pressure sensors (Ppods; Moum and Nash 2008; Thomas et al. 2016) were deployed on landers at five locations. Two of the landers were instrumented to observe near bed currents, turbulence, and seabed roughness using a suite of acoustic Doppler velocimeters (ADVs), high-resolution ADCPs (2 MHz), and high-frequency seabed imaging sonars.

Time series measurements of turbulence were acquired by several methods. As noted above, some five-beam ADCPs resolved turbulent stresses (Guerra and Thomson 2017). Temperature microstructure was measured along mooring lines and landers using χ pods (Moum and Nash 2009). A newly developed instrument for this experiment, the GusT (Becherer et al. 2020), was equipped to measure temperature and velocity microstructure as well as pressure and instrument orientation, pitch, roll, and acceleration. Approximately 80 GusT instruments were broadly deployed on moored and shipboard platforms, providing greatly enhanced coverage of turbulence over the inner shelf.

Surface gravity wave directional spectra were measured using Sofar Spotter buoys (Raghukumar et al. 2019) at 18 locations at the study site, and one miniature wave buoy near Point Sal. In addition, a suite of meteorological measurements (wind speed and direction, air temperature, atmospheric pressure, relative humidity, and shortwave radiation) were made from a mooring near Point Sal (Fig. 2) as well as from two locations on land near Oceano and Vandenberg.

Ship and small boat sampling. During two intensive operations periods (IOPs) in early September and mid-October (hereinafter IOP1 and IOP2; Fig. 3), as many as three ships (R/Vs *Oceanus*, *Sally Ride*, and *Robert Gordon Sproul*) and three small boats (R/Vs *Kalipi*, *Sally Ann*, and *Sounder*) conducted coordinated surveys within the study site, designed to resolve processes of interest. All vessels were equipped with downward-looking ADCPs and profiling conductivity–temperature–depth (CTD) instruments. Some ships were also equipped with echosounders, turbulence profilers (VMP-250, χ pods, and GusTs), fluorometers, and meteorological sensors. Bow-chains were deployed from the R/V *Sally Ride* and the R/V *R. G. Sproul* and measured temperature, salinity, and turbulence with high resolution vertically (1 m) and in time (sampling frequency: 2-8 Hz) in the upper 20 m of the water column. The R/V *Sally Ride* conducted over 5,100 vertical profiles using the VMP-250, while the R/V *Oceanus* equipped with a towed CTD installed with a GusT probe, attached at the leading edge of the CTD (Becherer et al. 2020) conducted over 4,200 profiles. The R/V *R. G. Sproul* conducted over 3900 profiles with a towed CTD.

Surface drifters. During the IOPs, on 14 separate days, approximately 30 drifters were deployed from small boats on daily (or longer) missions (Fig. 4) that were designed to target specific processes—for example, along- and across-shore transport and dispersion (Spydell et al. 2021), flow around the headland (Point Sal), and mapping surface vorticity and divergence (Spydell et al. 2019). All drifters were equipped with GPS and had real-time tracking capability. Most drifters measured surface temperature. Some were designed to directly measure surface vorticity. Others were equipped with sensors to measure surface shear and turbulence, wave statistics, and meteorological fields (Thomson 2012).

Remote sensing. During ISDE, a wide range of remote sensing observations were collected from research aircraft, small unmanned aircraft systems (sUAS), land- and

ship-based platforms, and satellites. During the IOPs, two airplanes conducted surveys of the entire study site. Sensors included thermal infrared cameras, optical cameras, hyperspectral cameras, interferometric synthetic aperture radar (InSAR), Modular Aerial Sensing System (MASS; Lenain and Melville 2017), and light detection and ranging (lidar). During these periods, sUAS deployed from land and from ships were equipped with optical cameras to focus on small-scale processes such as rip currents, and interactions between rip currents and internal bores. Surface winds and mean-square slope were estimated using the MASS (Lenain et al. 2019) along the track of the aircraft.

Four marine radars and a coherent imaging radar (all X band) were deployed from towers along the coast during the entire field experiment, with footprints that covered the entire study site (Fig. 2). A coherent marine radar was also operated from R/V *Oceanus*, and another marine radar was on board the R/V *Sally Ride*. Data from these systems were processed to focus on surface gravity waves as well as longer-time-scale processes, such as tracking internal waves and bores propagating to the coast, rip currents, and buoyant fronts and eddies and instabilities. In addition, spaceborne X-band and C-band SAR and optical satellite images of the study site were collected during the study period.

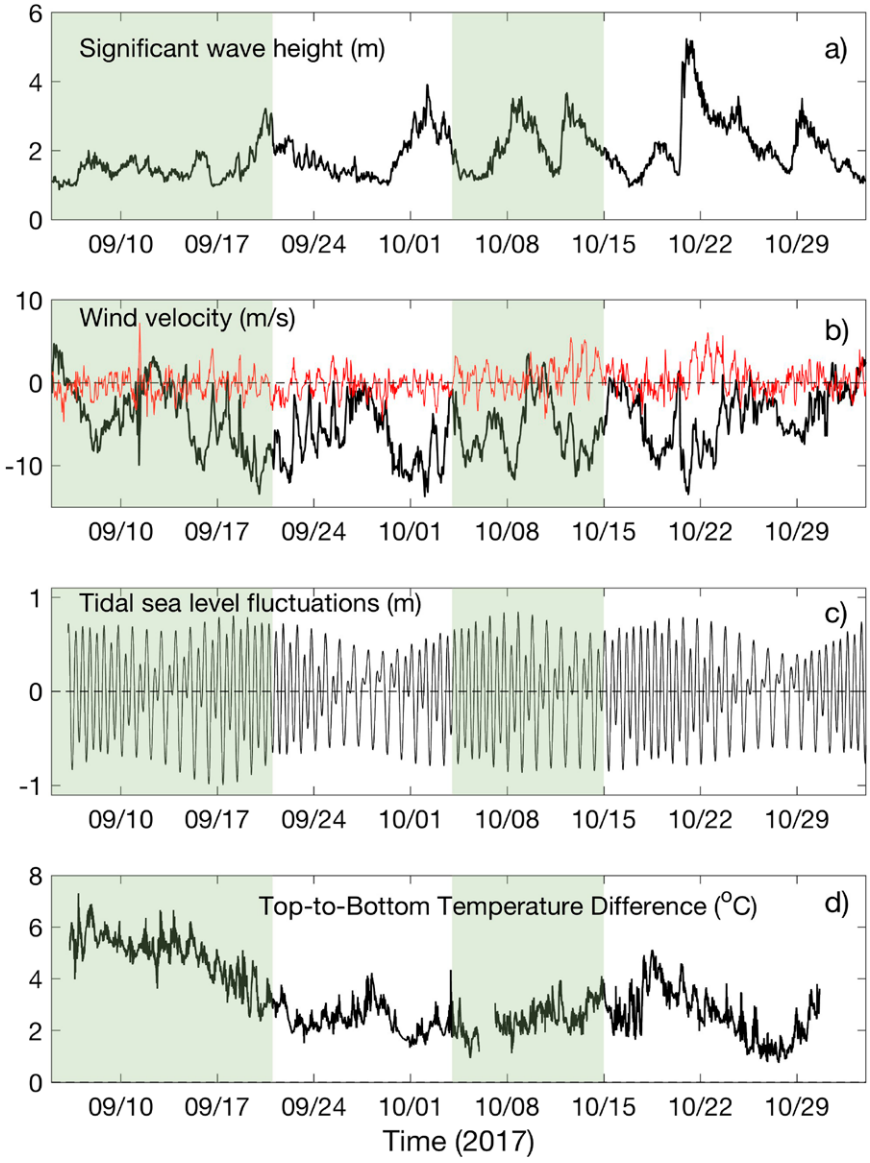

Fig. 3. Summary of conditions during the Inner-Shelf Dynamics Experiment. (a) Significant wave height. (b) Wind velocity rotated into primary (black) and secondary (red) coordinates; negative winds in the primary direction are upwelling favorable. Wave and wind data are from NDBC Buoy 46011 (Santa Maria). (c) Tidal sea level variations pressure measurements at the 50 m lander at Oceano (Fig. 2). (d) Top-to-bottom temperature difference at the 50 m mooring at the Oceano (Fig. 2). Periods of ship, small boat, airplane, and drifter surveys [intensive operations periods (IOPs)] are indicated by green shading.

Conditions during the experiment. Waves were small during the first IOP (significant wave height, Hsig < 2 m; Fig. 3a). Wave heights were variable in October, with Hsig exceeding 3 m during the second IOP and exceeding 5 m on 21 October. Winds were principally upwelling favorable during the experiment with several relaxation events (Fig. 3b). Strong diurnal wind variability was also apparent. Tides were mixed semidiurnal with a peak range of about 1.8 m (Fig. 3c). Stratification was strongest during the first half of September and was

reduced and variable during the remainder of the experiment (Fig. 3d). At a water depth of 50 m, the associated mode-one, linear internal wave speed ranged from 0.3 to 0.15 m s^{-1} (McSweeney et al. 2020b).

Modeling program

The ISDE modeling program centered on realistic and process-based hydrodynamics spanning a range of model hindcast, forecast, and sensitivity studies. The overall approach is briefly described here with more complete methodology provided elsewhere (Suanda et al. 2016; Kumar et al. 2019). The core modeling program consists of the open-source Rutgers Regional Ocean Modeling System (ROMS) and Simulating Waves Nearshore (SWAN) models, integrated in the Coupled Ocean–Atmosphere–Wave–Sediment Transport Modeling System (COAWST; Warner et al. 2010; Kumar et al. 2012). ROMS is a three-dimensional, bathymetry-following, hydrostatic numerical model (Shchepetkin and McWilliams 2005, 2009) with a long history of coastal applications (Olabarrieta et al. 2011; Kumar et al. 2015, 2016; Wu et al. 2020). SWAN is a third-generation, spectral wave model, which simulates shoaling, refraction, energy input from winds, and energy loss from whitecapping, bottom friction, and depth-limited breaking (Booij et al. 1999).

The model system is configured as a series of one-way, offline, nested grids. The outermost parent grid has resolution of 1/30° (Veneziani et al. 2009) covering the eastern Pacific Ocean from the Baja Peninsula, Mexico to Vancouver, Canada (L0). Subsequent child simulations have resolutions of 1 km (L1), 600 m (L2), 200 m (L3), 66 m (L4), and 22 m (L5), resolving processes from the continental slope and shelf break through the inner shelf and a bulk representation of the surfzone transition region (Fig. 5). Surface atmospheric forcing is taken from a nested Coupled Ocean–Atmosphere Mesoscale Prediction System (COAMPS) model (Hodur et al. 2002; Doyle et al. 2009). Tides are applied as boundary forcing on the L2 domain through harmonic sea level and barotropic velocities from the Advanced Circulation (ADCIRC) tidal model (Mark et al. 2004).

All modeled variables are stored hourly, spanning multiple years of simulation available through the data archive (Table 2). The nested model configuration was used to create a multiscale coastal forecasting system, coincident with the field experiment September–October 2017. Sensitivity tests and adjoint modeling were also conducted to determine the relative importance of initial and boundary conditions from the parent grid, and surface forcing.

Simulated hydrodynamics mirrors the ISDE field campaign focus; the regional transition between summer and fall determined by the prevailing atmospheric conditions (e.g.,

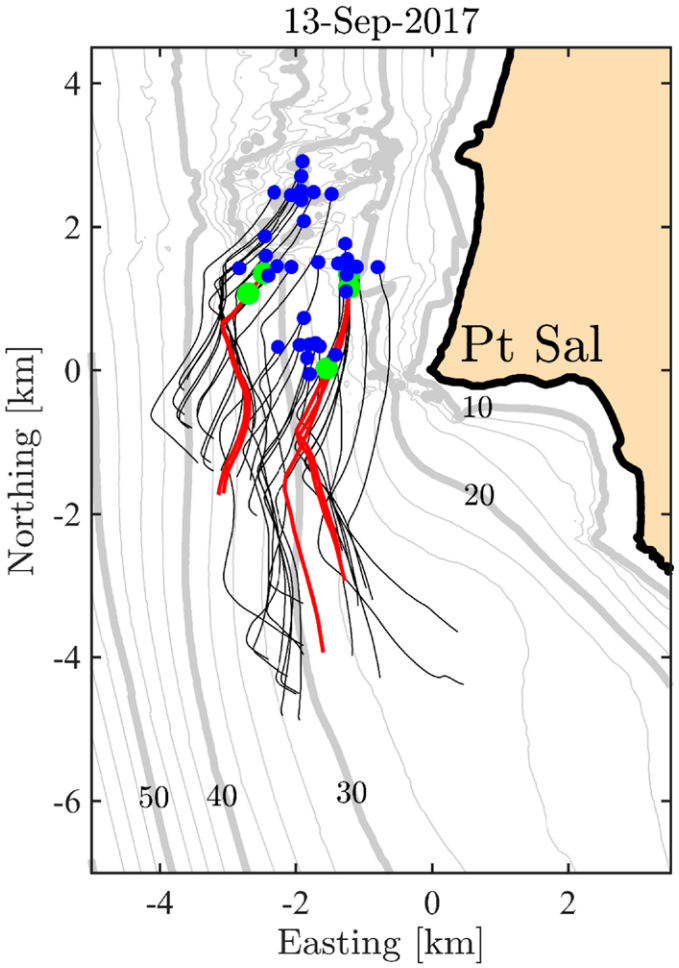

Fig. 4. Surface drifter tracks on 13 Sep 2017. Thirty-three CODE (black tracks) and five SWIFT (red tracks) drifters were released in 20–30 m water depths at approximately 0800 local time and sampled for approximately 5 h. Release locations are blue and green dots for CODE and SWIFT drifters, respectively. CODE and SWIFT drifters sample the top-1-m horizontal flow. Bathymetry is contoured at 10 m intervals (labeled thick gray contours) and 2.5 m intervals (thin gray contours). Two internal bores cause the two distinct "kinks" in the tracks. Adapted from Spydell et al. (2021).

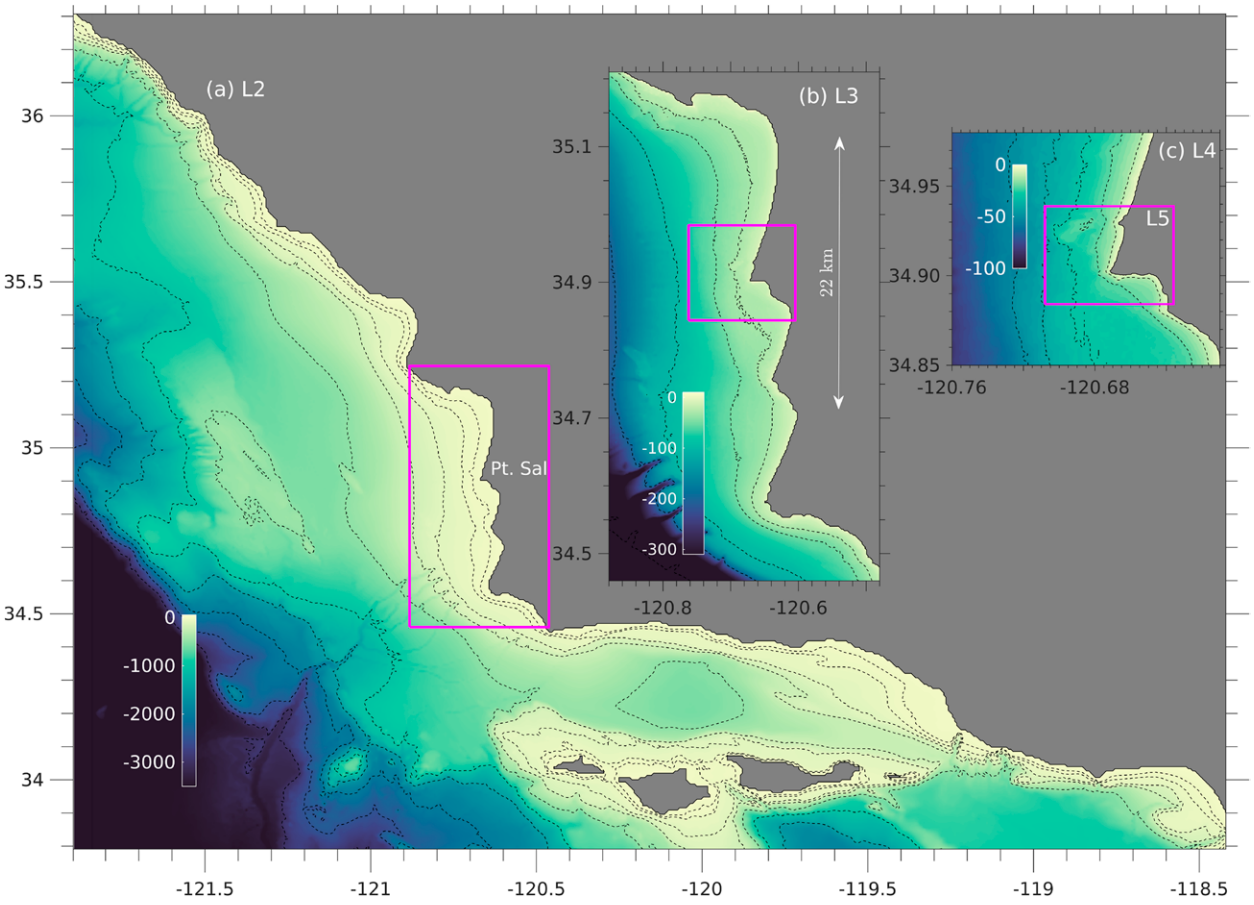

Fig. 5. Nested Regional Ocean Modeling System grids (L2, L3, L4, L5) and observation locations: (a) second-level nested grid (L2, resolution: 600 m). Color bar is the water depth *h* in meters; (b) L3 grid (resolution: 200 m), and (c) L4 grid (resolution: 66 m). In (a) dashed black lines are depth contours of 30, 50, 100, 200, 500, 1,000, 1,500, 2,000, 2,500, and 3,000 m. Parent grids L0 and L1 are shown elsewhere (Suanda et al. 2016).

Dorman and Winant 2000; Melton et al. 2009). A continued emphasis of the model simulations has been comparison against historical and ISDE observations. Model–data comparisons have spanned subtidal water-column temperature and velocity statistics at both outer- and inner-shelf mooring locations (Suanda et al. 2016; Kumar et al. 2019), to semidiurnal tidal band variability on the inner shelf including barotropic (Suanda et al. 2016) and baroclinic tidal oscillations (Suanda et al. 2017; Kumar et al. 2019). These studies document favorable model–data correlation, and reliable simulation of time-mean water-column vertical structure, large-scale sea level gradients, and water-column velocity.

Forecasting during the experiment. An experimental forecasting system for the inner-shelf circulation around Point Sal was operational from 1 September to 30 November 2017 to assist the field experiment of ISDE. Forecast of ocean conditions were conducted daily through the downscaling of several nested COAWST simulation grids (L0 → L1 → L2 → L3), each forced with the COAMPS 2-day atmospheric forecasts at hourly resolution. Comparisons of the field

Table 2. Model hindcasts conducted in the ISDE and made available as part of data archive.

Date range	Duration	Seasons encompassed	Grids	Validation and further info.
1 Jun–1 Aug 2000	60 days	Upwelling/summer	L0–L4	Suanda et al. (2016, 2017)
1 Jun–1 Aug 2015	60 days	Upwelling/summer	L0–L4	Kumar et al. (2019)
1 Jul–1 Dec 2017	180 days	Summer–fall transition	L0–L5	Fertitta (2019), Ahn (2019)

observations to the model forecasts showed that COAWST at 200 m grid resolution has significant skill in simulating near-surface temperature (not shown here).

Ensemble modeling to determine the relative importance of initial, boundary, and surface forcing. To further diagnose the dynamics underlying the model forecast skill, ensemble simulations of the COAWST Point Sal modeling framework were generated with different configurations of boundary and surface forcing conditions. The ensemble was used to quantify the sources of predictability (e.g., deterministic vs internal variability) that originate from knowledge of the open-ocean boundary conditions, surface forcings and initial conditions. The initial conditions result in little skill beyond a few days and that the largest fraction of dynamical skill is associated with knowledge of the surface and open boundary conditions (Sutherland et al. 2011; Giddings et al. 2014). These findings suggest that direct data assimilation to initialize the ocean model state may not be required for an operational ocean forecast at the inner-shelf spatial and temporal scales.

Adjoint modeling to identify the role of physical processes. The efficacy of the ROMS simulations is controlled by model inputs such as initial and boundary conditions, and model parameterizations to be specified a priori. All circulation aspects (e.g., "Background" section) as represented in the model are therefore sensitive to variations in any or all of these factors, and parameters can be quantified using the ROMS adjoint. Specifically, the sensitivity of any scalar function of the circulation to model parameter and input variability can be computed from a single integration of the adjoint model, by utilizing a state-of-the-art four-dimensional variational data assimilation system which forms part of the ROMS framework.

Two specific processes have been the focus of adjoint sensitivity analyses on the L3 grid: the onshore semidiurnal baroclinic energy flux associated with internal waves (e.g., Kumar et al. 2019), and the vertical (over the water column) transfer of horizontal momentum through vertical mixing. For the former, a specific focus has been on the sensitivity to variations in the formulation of bottom drag, bathymetry and vertical mixing parameterizations. In the case of the vertical transfer of momentum, an index based on the gradient Richardson number (i.e., the ratio of the squared buoyancy frequency to the squared velocity shear) is used to explore how each ocean state component controls vertical transfer of momentum. These numerical studies also serve as a useful prelude to the assimilation of the field observations into ROMS since they provide the spatiotemporal sensitivities of scalar functionals to the circulation fields.

Processes investigated and preliminary findings

Field measurements from various in situ sensors and remote sensing platforms, combined with numerical model results are used to highlight four important physical processes in the Santa Maria basin: internal wave dynamics from the midshelf to the inner shelf, flow separation and eddy shedding off Point Sal, offshore ejection of surfzone waters from rip currents, and wind-driven subtidal circulation dynamics. In addition, the capability of using a few wave sensors to create a regional wave forecasting system is discussed.

Internal wave dynamics. Observed nonlinear internal waves (NLIWs) included steep bores, undular bores, and high-frequency waves of elevation and depression. Internal bores propagated into the region every 6 h (McSweeney et al. 2020b) and were detectable in both in situ and remote observations. Data from satellite SAR and land- and ship-based radar stations demonstrate that internal bores were alongshore coherent of order tens of kilometers, with additional short-scale horizontal variability (Fig. 6). This alongshore coherence decreased toward shore (see BAMS-RadarAnimation-IW.mp4 in the online supplementary information;

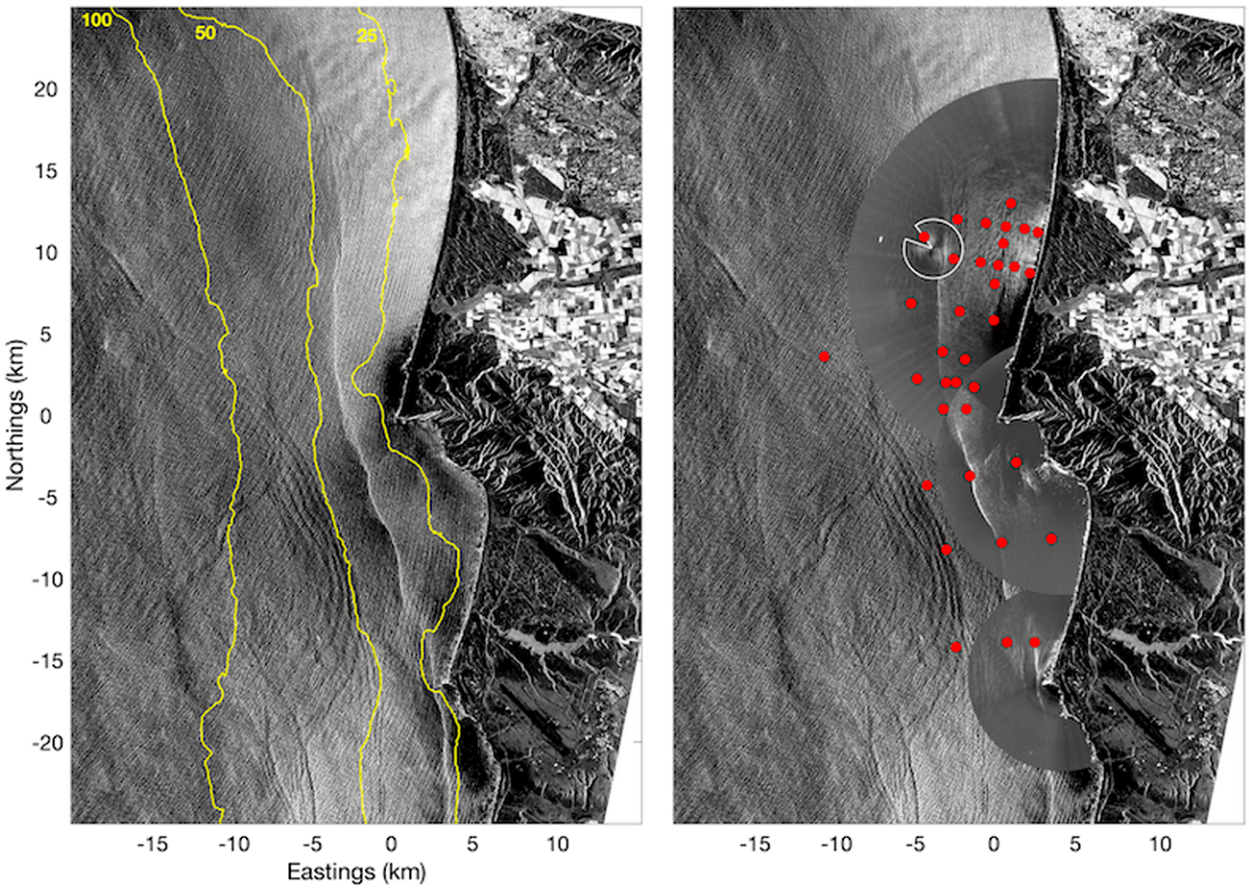

Fig. 6. (left) COSMO-SkyMed X-band synthetic aperture radar (SAR) satellite image at 0158:49 UTC 9 Sep 2017, showing surface signatures of multiple internal waves. Yellow contours indicate the 25, 50, and 100 m isobaths. (right) Same SAR image overlaid with data from three land-based X-band radar stations and one shipboard X-band radar (outlined in white). Red dots indicate mooring locations. COSMO-SkyMed Product Agenzia Spaziale Italiana (ASI) 2017 processed under license from ASI. All rights reserved. Distributed by e-GEOS.

https://doi.org/10.1175/BAMS-D-19-0281.2; McSweeney et al. 2020a), contributing to nearshore semidiurnal temperature variability (Feddersen et al. 2020).

As internal waves propagated into shallower water, their evolution depended on the shelf stratification and background shear. The pycnocline depth ahead of a bore was found to influence the evolution of frontal steepness (McSweeney et al. 2020a). Cross-shore mooring transects illustrate that an internal bore can maintain a sharp front from the 150 to 9 m isobath, while higher-frequency internal waves evolve over shorter distances (Fig. 7). The high space–time resolution of the continuously sampling shore-based radars provided detailed observations of NLIW transformations, including alongshore variability, speed tracking (Celona et al. 2021), and along-crest scalloping (see BAMS-RadarAnimation-IW.mp4 in supplementary information). Other interesting observations were internal wave–wave merging, wave packet stretching, NLIW reflection, and breaking.

Turbulence dissipation estimates revealed elevated turbulence behind the internal bore front (Figs. 7a, 8), suggesting that NLIWs generate strong mid-water-column mixing due to shear and/or convective instabilities. Elevated near-bottom dissipation from internal bores was also observed with an upward-looking ADCP, which shows an increase of two orders of magnitude in turbulent kinetic energy dissipation (E) after a bore passage (Fig. 7b). Microstructure observations from towed and profiling shipboard instrumentation (VMP-250 and GusTs) and near-surface drifters (Thomson 2012) have allowed for the first comprehensive mapping of the turbulent dissipation rates over the inner shelf, spanning bathymetrically smooth and headland-type region. Shelf variability of dissipation rate is further described in the "Discussion" section.

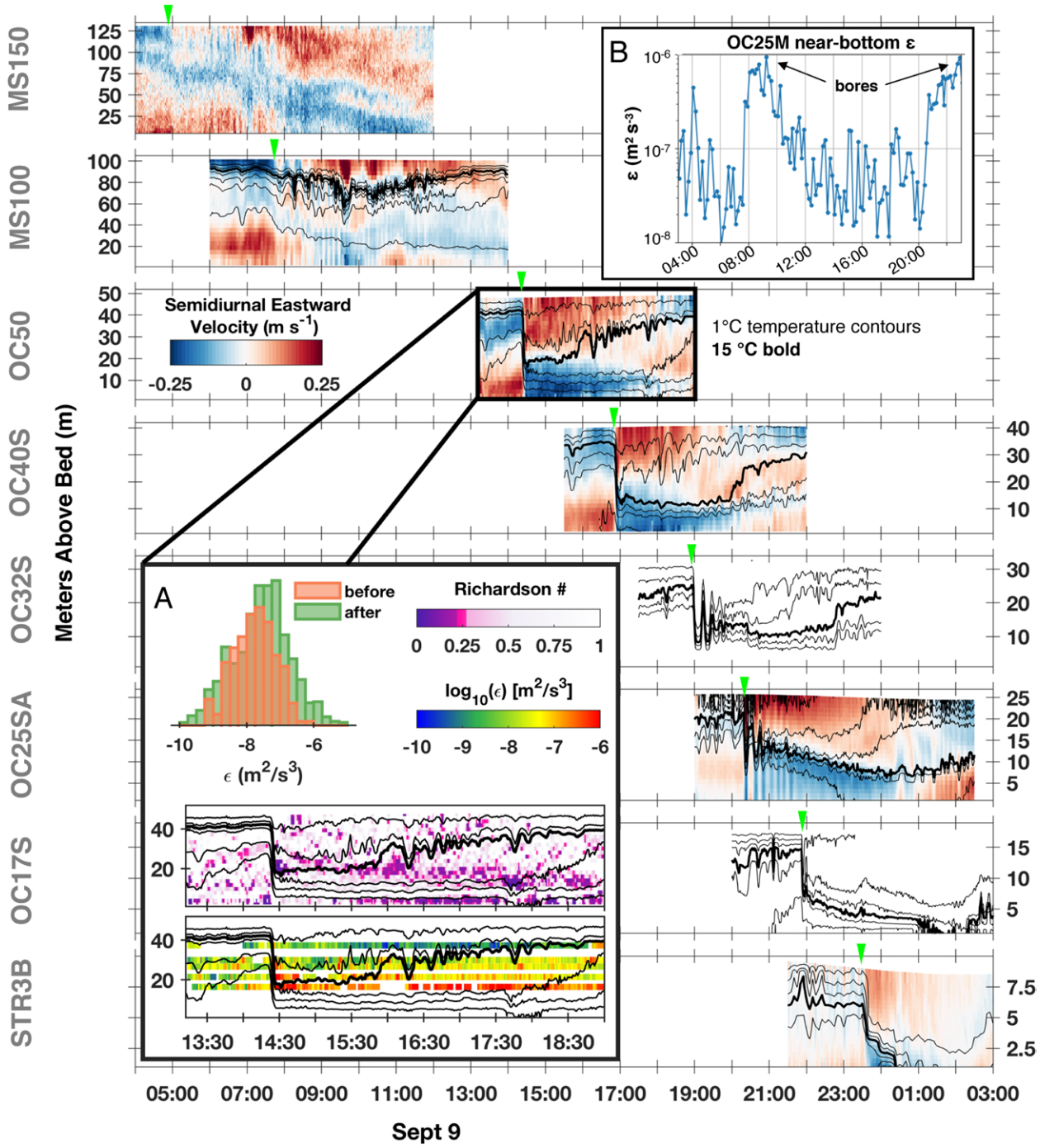

Fig. 7. (top to bottom) Data from a cross-shore transect of moorings, ranging from (top) 150 to (bottom) 9 m depth. Data include 16 h high-pass-filtered eastward velocities (colored; positive indicates onshore flow) and 1-min-resolution temperature data (contoured at 1°C intervals; 15°C is bold). Internal wave arrivals are indicated with green triangles. (a) Zoom in on the OC50 mooring data, including temperature contours, (middle) the Richardson number [Ri = the ratio of the squared buoyancy frequency to the squared velocity shear], and (bottom) estimates of *E* ($m^2\ s^{-3}$) from the GusT turbulence probes, as well as (top) the probability density function of *E* values before and after the internal bore front. (b) Zoom-in on the OC25M mooring data, showing near-bottom (1–6 m above bottom) 10-min-averaged estimates of *E* from a modified ADCP structure function method (Scannell et al. 2017). Similar figures with internal wave arrivals are discussed extensively in McSweeney et al. (2020b,a).

Analogous to saturated waves in the surfzone, where broken surface gravity waves (bores) have amplitudes that are proportional to the water depth and energy loss depends on water depth and bathymetry slope, internal tides propagating into the inner shelf can reach a saturated state

(Becherer et al. 2021a,b). The internal tide saturation region starts where the incident internal tide amplitude becomes comparable to the water depth. This typically occurred at water depths between 40 and 80 m during ISDE. Inside the saturation range, the internal tide loses memory of the energy of the incident wave farther offshore, and energy and energy loss are functions only of stratification (vertical density gradient), water depth, and bathymetric slope. These dependencies allow for a simple parameterization of internal tide energy, energy loss, and mixing in the saturation region that has proven to be applicable generally to inner-shelf regions globally (Becherer et al. 2021a,b).

Nonlinear internal waves can drive strong thermal fronts in the inner shelf that are apparent from remotely sensed measurements. For example, aerial images of sea surface temperature and relative temperature from two airplane-mounted longwave infrared cameras (Figs. 8a,b; Melville et al. 2016) reveal an internal wave front that extends ~20 km alongshore and is relatively warm (1°C) offshore of the front compared to the water inshore. This NLIW temperature gradient is also evident from cross-front ship transects, which additionally show the internal bore vertical structure and elevated turbulence behind the front (Fig. 8c).

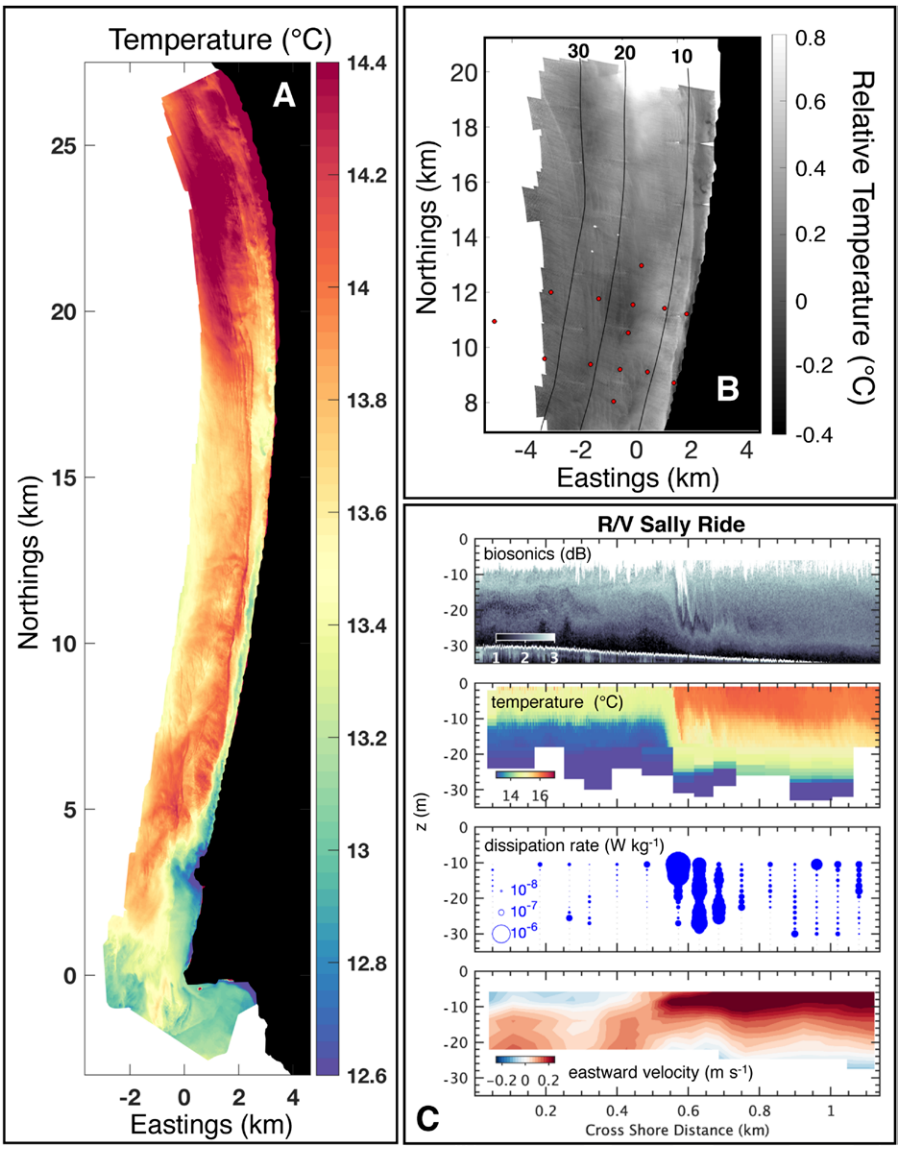

Fig. 8. Aerial views of an internal wave front, including (a) sea surface temperature and (b) relative temperature from plane-mounted longwave infrared (LWIR) cameras (MASS; Melville et al. 2016). (c),(top to bottom) Cross-shore transects of an internal bore from a ship survey, including biosonics from the ship's echosounder; temperature data from a bow-chain temperature profiler (top layer) and a towed CTD (bottom layer); dissipation rates from a VMP, and (eastward velocity from a pole-mounted, downward-looking ADCP.

Cross-shore velocities associated with internal waves can drive cross-shore transport of sediment. NLIWs create both onshore and offshore near-bed velocity pulses, with shoreward-propagating elevation (depression) waves advecting fluid shoreward (offshore) near the bed. Observed near-bed, cross-shore currents demonstrate that high-frequency elevation waves generate bed shear stresses that exceed the critical threshold for sediment motion (Fig. 9), and suspended particulates may not settle between internal waves within a packet (based on grab sample measurements of sediment size). Critical bed shear stress was estimated following Allen et al. (2018) (sand, d_{50} = 0.10 mm). Near-bed turbulence measurements

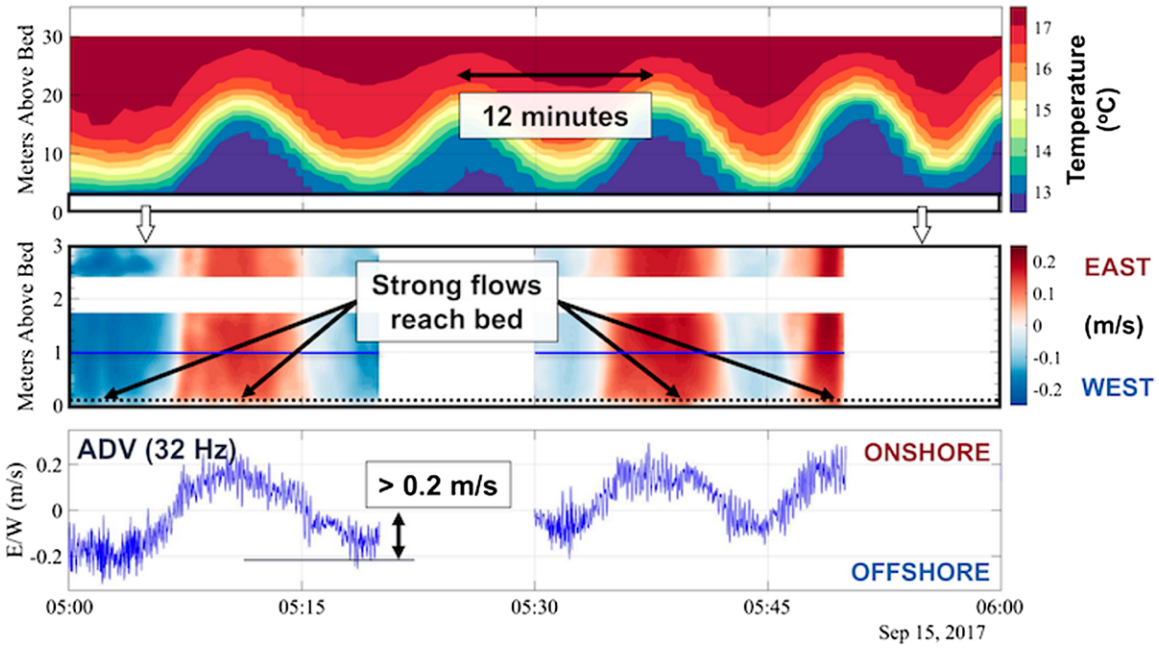

Fig. 9. (top) A 1 h temperature time series covering 5–30 m above the bed (mab) from a lander at 35 m depth shows a packet of high-frequency waves of elevation. (middle) East–west velocity profiles over the 3 mab (black box in the top panel) from a pair of up- and down-looking, pulse-coherent, high-resolution ADCPs show strong near-bed velocities during the same time. (bottom) East–west velocity component from an ADV located roughly 1 mab (blue line in the middle panel) show the amplitude of currents associated with the time scale (~12 min) of internal waves to be typically 4 to 5 times greater than the amplitude of currents associated with the time scale (~8 s) of surface gravity waves. The ADV and ADCPs logged for 20 min every half hour. The observed near-bed flows exceeded the critical threshold for sediment motion.

indicate an asymmetry in turbulence across the internal waves, partly due to inflectional instability in adverse pressure gradients and partly due to the residence time of fluid within an internal wave pulse, and this asymmetry may lead to a net onshore transport of sediment (Becherer et al. 2020).

To complement observations, regional numerical simulations were used to identify the potential generation region of tidally forced internal waves (Kumar et al. 2019). The model indicated negligible local shelfbreak barotropic to baroclinic energy conversion compared to persistent but spatially variable energy conversion at an offshore escarpment located 80 km from the continental shelf, with near- and supercritical bottom bathymetry relative to an internal tidal beam (Kumar et al. 2019).

Headland wakes at Point Sal during the inner-shelf experiment. Headland wakes at Point Sal are expected to exhibit considerable complexity. The incident flow on this asymmetric headland is a combination of tidal and low-frequency currents, potentially leading to asymmetric vorticity production on either side of the point (MacKinnon et al. 2019). Furthermore, the strong internal tide, soliton, and bore phenomena described herein ("Internal wave dynamics" section, Fig. 7) may interact in heretofore unknown ways with the shear and vorticity of wake eddies. Here, we report preliminary observations of headland wakes from the ISDE.

A headland wake SST feature is observed at 1042 PDT 11 September 2017 from an airplane equipped with the MASS package (Fig. 10c). Here, a cold (<15°C) water wake is seen at the tip of Point Sal streaming to the southwest (SW) for 1 km. The cold wake may be induced by enhanced turbulent mixing from the rough rocky bathymetry with colder water below or offshore advection of colder nearshore water. Depth-limited wave breaking on a 3-m-depth

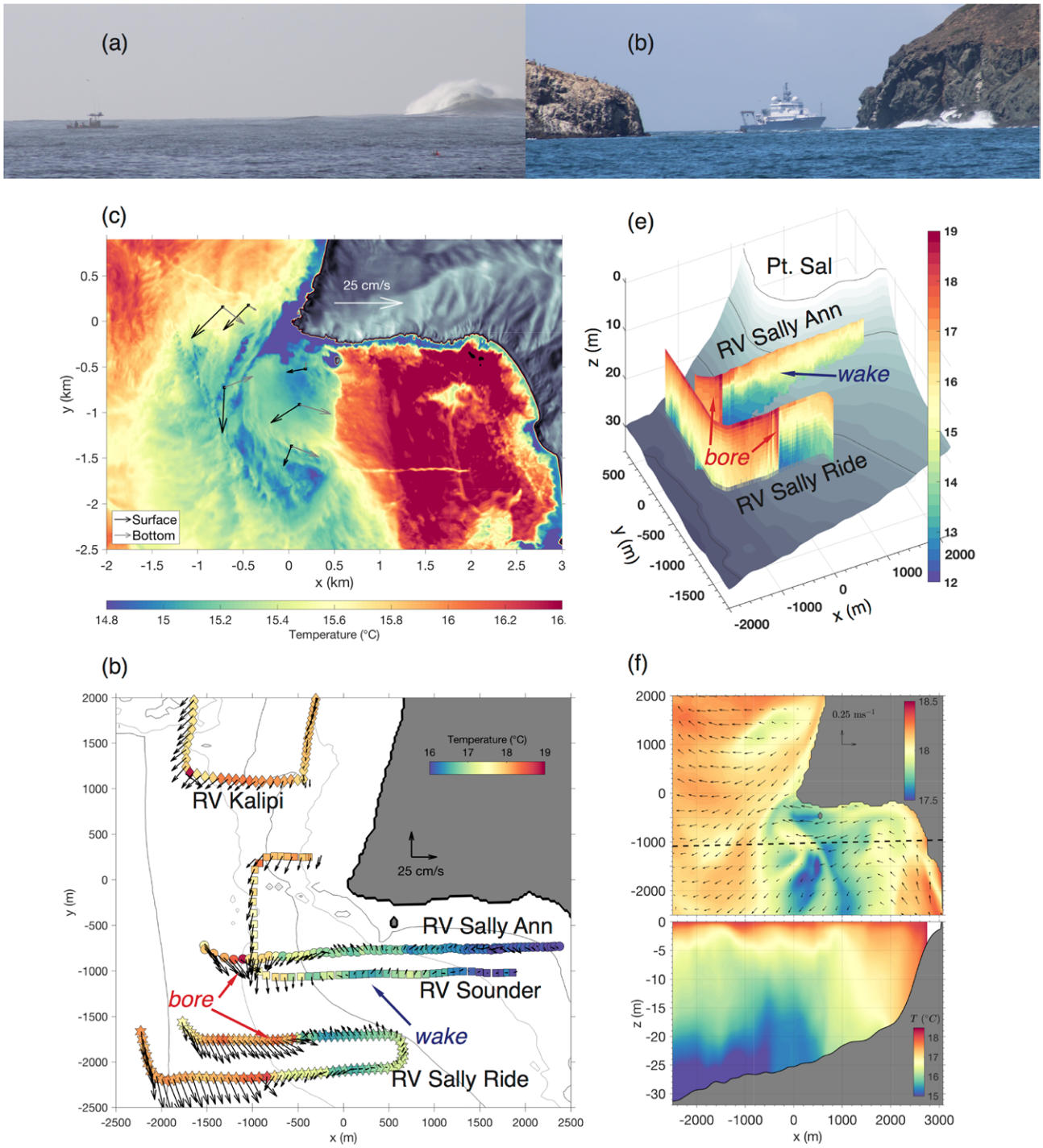

Fig. 10. Schematic of Point Sal headland wake sampling and modeling. (a) The R/V *Sally Ann* sampling within 100 m of Point Sal with wave breaking on offshore shoal in the background. (b) The R/V *Sally Ride* on an onshore transect toward Point Sal. (c) Aerial sea surface temperature near Point Sal at 1042 PDT 11 September 2017 from the airborne MASS system (Melville et al. 2016) in the east (*x*)–north (*y*) coordinate system with origin at Point Sal (34.9030°N, 120.6721°W). The color scale is set to highlight cold features streaming off of Point Sal. Note the curving streak of cold water emanating off of Point Sal. The near-surface (black arrows) and near-bed (gray arrows) ADCP velocities indicate regions of both convergence and vorticity consistent with the cold streak. A 25 cm s^{-1} velocity scale arrow is shown for reference. (d) R/Vs *Kalipi*, *Sally Ann*, and *Sally Ride* vessel surface temperature and near-surface velocity transects near Point Sal with overlaid bathymetry contours (15, 20, 25, and 30 m). The recirculation of the wake and the onshore-propagating warm bore are indicated. (e) Three-dimensional view of single R/Vs *Sally Ann* and *Sally Ride* temperature transects near Point Sal, indicating onshore-propagating warm bore and wake region in lee of Point Sal. (f) ROMS model at 1100 PDT 12 September 2017: (top) surface temperature and currents and (bottom) cross-shore temperature transect at the dashed line of the top panel. Note the colder water streaming off of Point Sal and the near-surface velocity arrows indicating a headland wake, recirculation, and vorticity.

rocky shoal 500 m west of Point Sal (see Fig. 10a) acts via vertical mixing as a secondary cold water source also streaming SW. The surface velocities west of Point Sal are SW at 0.15 to 0.2 m s^{-1} consistent with the spatial evolution of the cold wake. The headland wake also has smaller-scale features to ~100 m. After about 1 km, the cold wake bends southeast, consistent with surface velocities, for another 1 km as it warms and broadens before its signature disappears. Based on a surface velocity of 0.15 m s^{-1}, we hypothesize that the wake's leading edge was generated 3.75 h previously.

Multiple vessels transected near Point Sal on 13 September 2017; however, thick clouds prevented airplane observations. Transects over a 1.5 h (1130–1300 PDT) duration are shown in Fig. 10 together with sea surface temperature and shipboard ADCP surface velocities. The composite shipboard measurements reveal aspects of the wake structure. Upstream of the point, the flow is warm offshore and cooler inshore, with strong cross-shore shear in the southward flow (Figs. 10a,b). This cross-shore shear is in the sense of positive (cyclonic) vorticity. Headland flow separation transports vorticity offshore, producing the ~1-km-sized cyclonically rotating eddy visible both in the airborne image and the shipboard current data. Near x = 0 m, the R/V *Sally Ann* velocity measurements show recirculation as cooler water is drawn back toward the headland. Subsurface, the wake reduces stratification and isopycnal tilt as seen for example both in the *Sally Ann* transect near x = 0 m (Fig. 10e) and in the model transect (lower portion of Fig. 10f). Mooring data (not shown) reveal a strong tidal component to the flow, making wake generation an often regular tidal cycle event. Kovatch et al. (2021) further explore headland vorticity generation.

A defining feature of this field program is the capability to observe the superposition of multiple different physical features, in complex and often interacting ways. Here, onshore-propagating nonlinear tidal bores and solitons often propagated through wakes. An example of which is seen in Fig. 10e). Warm water in the offshore end of both the R/V *Sally Ann* and *Sally Ride* transects were bounded by very sharp gradients. The onshore-propagating warm bore was at least 10 m thick with 0.2–3 m s^{-1} onshore velocities. These warm bores were similar to those seen around Oceano (McSweeney et al. 2020b) and they propagate deep into the bay in the lee of Point Sal (not shown).

The Point Sal region ROMS simulations (described in more detail in the "Modeling program" section) also show similar headland wake generation (Fig. 10f). For 1100 PDT 12 September 2017, the model has a headland wake but no incident warm bores. Just north of Point Sal, flow is down-coast to the SSW and the near-shoreline waters are cooler, which separate from Point Sal and propagate in a cold streak to the SW before curving SE after 1 km. This overall pattern is consistent with the SST and ADCP velocities in Fig. 10c. At the south coast of Point Sal, the westward velocities bring colder water that merges with the wake. On the cross-shore transect, isotherms can be significantly displaced leading to regions of reduced or increased stratification consistent with Fig. 10e. Overall, the modeled headland wake features are qualitatively consistent with the observations.

Exchange and interactions with the surfzone. One objective of the ISDE was to quantify the role of the surfzone as an onshore "boundary condition" to the shelf. In particular, it is not known how cross-shore exchange, or the magnitude of onshore or offshore material transport, varies along a complex coastline. Furthermore, the extent to which shelf and surfzone processes, including rip currents and internal waves, influence each other is poorly understood.

To quantify bathymetric and transient rip currents, eddies, fronts, internal waves, and other processes in the surfzone to inner-shelf transition region, the team collected observations of temperature, salinity, turbidity, fluorescence, radar backscatter, and velocities from a range of complementary observational platforms: moorings in 5–10 m water depth, drifters,

land-based X-band radar, sUAS-based visible imaging, manned aircraft thermal IR and visible imaging, and along-coast surveys coordinated from multiple vessels. On many occasions the aircraft, small-boat, and shore-based radar/sUAS teams used real-time visual or instrumental observations to target interesting events opportunistically. The resulting dataset is rich with signatures of processes driving exchange between the surfzone and inner shelf, with strong variations at a range of space and time scales.

Particularly striking are events in which rip currents appear to collide with shoreward-propagating internal waves and fronts. On numerous occasions fronts or internal waves were observed in radar or airborne data to reach the surfzone edge (several hundred meters from the shoreline), sometimes appearing to "wrap around" rip-current plumes that extended up to several surfzone widths offshore (up to 1 km from the shoreline; Fig. 11b).

Aircraft thermal infrared observations captured numerous signatures of plumes originating in the surfzone interacting with fronts and internal waves on the shelf (Fig. 11a). These signatures were strongest (1°C) in the infrared maps of the ocean skin temperature during periods of relatively weak winds, and thus were complementary to the X-band radar measurements, which require moderate wind conditions. A noteworthy observation was that the surface temperature of rip current plumes often was distinct (either cooler or warmer) from surface temperatures on the shelf. Cool plumes were more prevalent in the morning (Fig. 11a; also see Grimes et al. 2020b) and warm plumes were more common in the afternoon (Hally-Rosendahl et al. 2014; Moulton et al. 2021). At times, both cool and warm plumes were present (not shown), possibly as a function of location relative to headland topography, or as a result of differential transport by shore-intersecting internal bores. Preliminary results suggest that cross-shore length scales of cool plumes are smaller than warm plumes, and that the plume temperature also controls vertical structure, with cool plumes subducting (e.g., Kumar and Feddersen 2017c; Grimes et al. 2020a) and warm plumes spreading in a thin layer near the surface (Moulton et al. 2021). Infrared signatures of shoreward-propagating fronts were observed to reach the surfzone and interact with rip currents (Fig. 11a; $y < -5$ km), similar to the X-band radar observations.

Hydrodynamic features such as rip currents, fronts, and internal waves appear in X-band radar imagery as areas of increased or decreased backscatter intensity. Figure 11b shows a large rip current (high intensity feature at $y = 8.1$ km) appearing to interact with an onshore-propagating internal bore (visible as alongshore bands of high and low backscatter). An optical image of the same interaction (Fig. 11c) from a sUAS shows a white foam line carried by the internal bore as it bends around the rip current plume (with the location of the foam line indicated with arrows). Temporally overlapping mooring data show temporal patterns in the east–west velocity and temperature fields associated with the passing features observed in the radar imagery (Figs. 11d and 11e, respectively; the blue dot indicates sensor location in Fig. 11b). The bright linear radar feature (transecting the blue dot) is collocated with the back face of a cold pulse at depth (5°C cooler than the surface water; see Fig. 11e) lasting around 6 h at the sensor location. These and other mooring data indicate that internal waves alter the stratification outside of the surfzone on relatively short time scales. This rapid stratification of an unstratified region is expected to influence offshore material transport by rip currents (Kumar and Feddersen 2017b,c,a).

Subtidal, wind-driven, mesoscale, relaxation. Subtidal motions and water-column structure at the study region are dominated by wind forcing, but an along-shelf pressure gradient is also important for driving northward currents over the inner to midshelf in this region (Winant et al. 2003; Cudaback et al. 2005; Melton et al. 2009; Fewings et al. 2015). This along-shelf pressure gradient can be associated with prevailing winds in combination with local coastline topographic variability, wind relaxation events, or with remotely

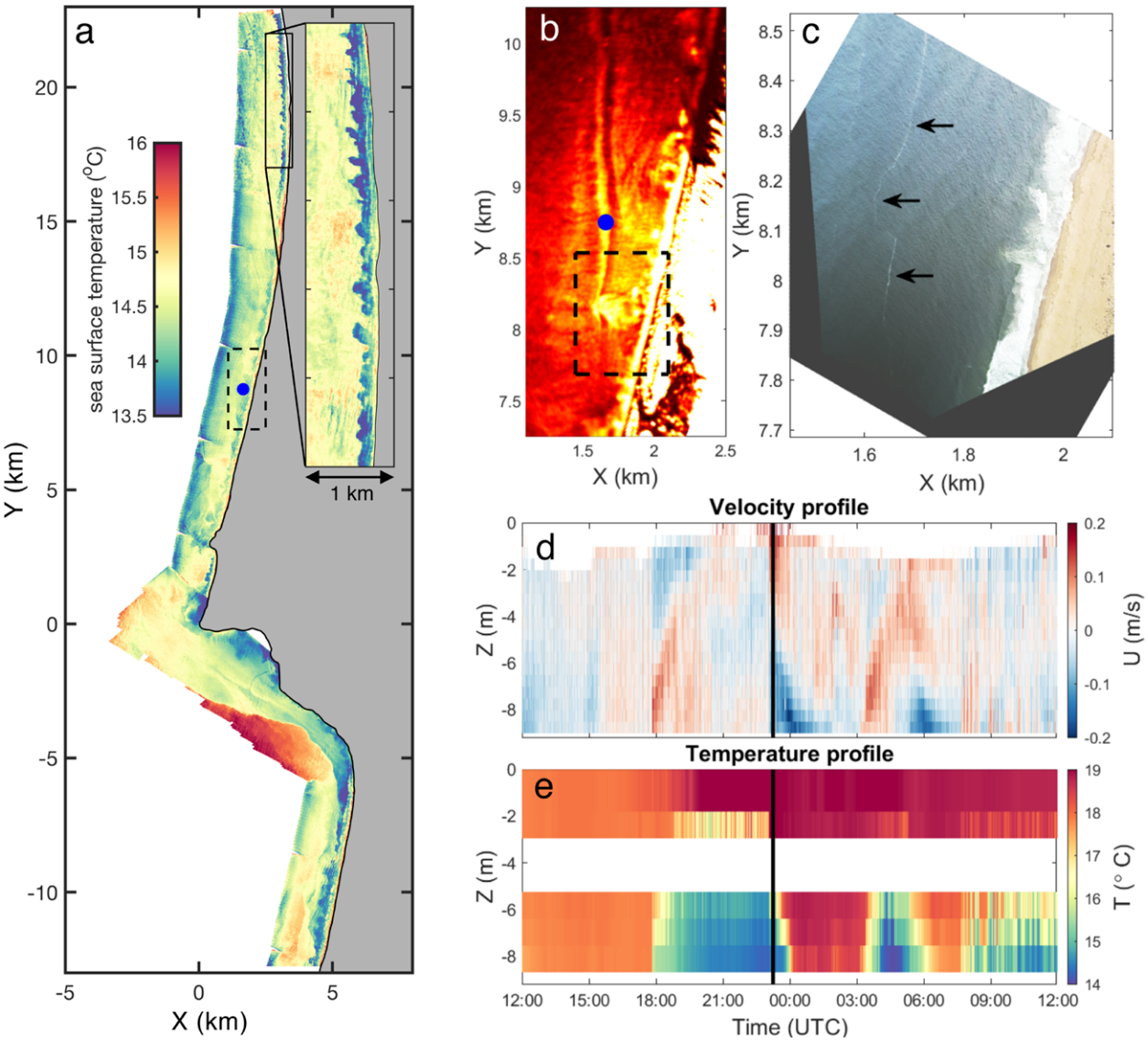

Fig. 11. Interactions between surfzone rip currents and internal waves on the shelf. (a) Airborne thermal infrared image (°C, calibrated with radiometer), taken on 15 Oct 2017 starting at 1639 UTC, composed of a mosaicked set of images from a continuous nearly 50-km along-coast transect centered at Point Sal (near y = 0 m). Cool "plumes" driven by rip currents (e.g., cool features emerging from the surfzone) with several-hundred-meter cross-shore scales at $0 < y < 22$ km and $-12 < y < -7$ km are observed, along with signatures of fronts and internal waves (e.g., strong frontal signature at $-4 < y < -6$ km). In the southernmost half of the image, a strong front was observed to intersect with plumes in the surfzone. Inset shows zoom to 1 km × 5 km region with cool plumes. Dashed box in (a) shows the location of the radar image in (b) and the blue dot shows mooring location in both panels. (b) X-band radar subimage. Dashed box in (b) shows the location of the sUAS image in (c). (c) Rectified visible image from sUAS. (d) Mooring time series of the east–west velocity profile. (e) Temperature vs depth time series for an event in which an internal wave [bright band in (b), white foam line in (c) indicated by arrows] intersected with a rip current [plumelike feature in (b) and (c) near y = 8 km] on 12–13 Sep 2017. The time of the radar image is shown with a vertical line in the velocity and temperature profiles. The gap in the temperature profiles in (e) from approximately z = –3 to –5 m is due to the loss of two temperature sensors during the deployment period.

generated coastal-trapped waves (Auad et al. 1998; Hickey et al. 2003; Melton et al. 2009; Washburn et al. 2011).

Here, we use a subset of the observations collected during the ISDE to focus on subtidal flows to the north of Point Sal, a region of relatively simple, planar continental shelf bathymetry, and around the three-dimensional point itself. We use 26 mooring–lander pairs that

measured water-column temperature and velocity using thermistors and bottom-mounted ADCPs, as well as water-column observations made during the two intensive observation periods (Fig. 3). We use water-column velocity measured from a downward-looking, 600 (1,200)-kHz ADCP mounted on a side pole from R/V *Oceanus* (R/V *Kalipi*).

Mooring, lander and wind time series are low-pass filtered to remove diurnal, semi-diurnal and shorter time-scale fluctuations. At each mooring, temperature anomalies are defined by subtracting the time-mean temperature at each mooring sensor across the entire moored array. These temperature anomalies are objectively mapped onto the study region (Fig. 12).

In this region, because along-shelf pressure gradients due to warm water to the south of nearby coastal promontories, most notably Point Conception, California, drive currents to the north even in the presence of substantial nonzero, upwelling-favorable winds, we define an upwelling pattern only when southward winds exceed 4 m s^{-1}.

The low-frequency wind forcing in this region is dominated by southward, upwelling-favorable wind events lasting 2–5 days (designated by blue lines in Fig. 12), separated by relaxations in the wind. An example upwelling event is constructed by averaging moored array and shipboard data over the period of the sampling from R/V *Oceanus* during 0311–1517 UTC 14 October 2017 (Fig. 12). The "C"-shaped ship transect around Point Sal took approximately 3 h to complete so was occupied five times in an effort to average out the strong influence of semidiurnal motions in this region. Note the relatively good agreement between the moored and ship-based velocity fields, reflecting the efficacy of averaging the ship-based data. The R/V *Kalipi* completed 3 C-shaped surveys closer to Point Sal during daylight hours on 14 October 2017.

The upwelling circulation is dominated by a southward, horizontally and vertically sheared, coastal upwelling jet that encounters the coastal promontory at Point Sal (Fig. 12). Upstream of Point Sal, near 35°N, the coastal upwelling jet flows southward with a maximum speed of about 0.15 m s^{-1} over the 40 m isobath. The southward transport in the upwelling jet across the cyan dashed line

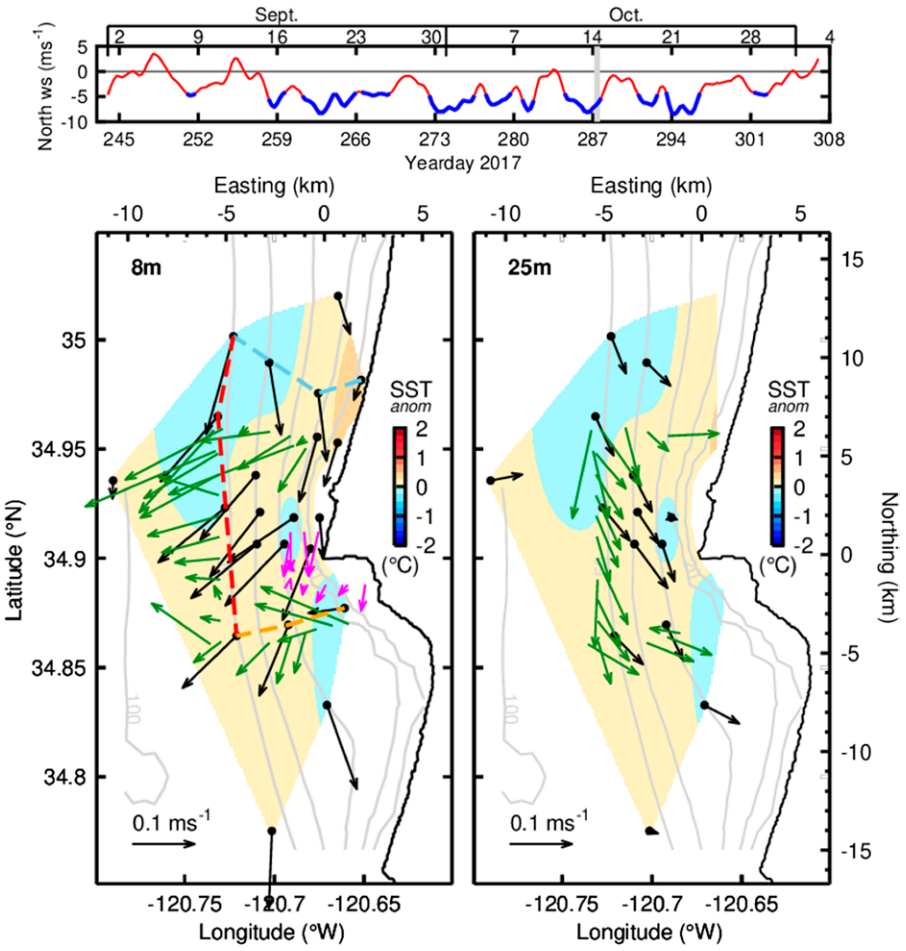

Fig. 12. (top) North–south wind speed (m s^{-1}) from NDBC buoy 46011. Periods when winds are upwelling-favorable (southward) and greater than 4 m s^{-1} are highlighted with a thick blue curve. (bottom) Average (left) near-surface (1 m) temperature anomalies from objective mapping of moored sensors, and currents (8 m) and (right) 25 m currents during an upwelling-favorable wind event on 14 Oct 2017. Currents measured by the mooring array are in black and those from repeated ship surveys around Point Sal are in green (R/V *Oceanus*) and magenta (R/V *Kalipi*). Dashed colored lines indicate sections for computing fluxes. Isobaths are plotted every 10 m to 50 m and then the 100 m isobath is plotted.

in Fig. 12 is $1.32 \pm 0.10 \times 10^4$ m^3 s^{-1}. The coastal upwelling jet is advecting cold water south along the midshelf north of Point Sal, with warmer water inshore north of Point Sal due to southward advection of warm water formed in the lee of next embayment to the north (Port San Luis, Avila Beach). Note the weak flow at the 100 m mooring, indicating that this site is more influenced by a northward along-shelf pressure gradient set up by the large-scale pattern of warm water to the south (Suanda et al. 2016) than by wind-driven motions.

The cross-shelf flow north of Point Sal shows offshore surface flow less than 0.05 m s^{-1} that, when summed over the 15-m-thick upper layer yields an offshore flux of 0.75 m^2 s^{-1}. Equating this to the theoretical offshore surface Ekman transport yields an estimate of the wind speed of 6 m s^{-1}, consistent with the observed wind speed during this upwelling event. The onshore compensatory, cross-shelf flow, evident in the 25 m vectors, is found beneath the offshore surface Ekman flux.

Downstream of Point Sal, a similar southward coastal upwelling jet exists with a maximum over the 30–70 m isobaths with northward deep flow at the offshore end of the section. The southward flow across the orange dashed line in Fig. 12 is $0.87 \pm 0.10 \times 10^4$ m^3 s^{-1}. The cross-shelf surface flow is offshore, but stronger than that found north of the point due to the deflection of the coastal upwelling jet by the point. The onshore compensatory flow is found throughout the section beneath 20 m depth. Near Point Sal (34.9°N), near surface (8 m) flow is strongly offshore, a result of the coastal upwelling jet encountering the change in coastline and isobaths associated with the point. Summing the flow across an along-shelf section along the 50 m isobath between Oceano and Vandenberg (red dashed curve in Fig. 12) yields an offshore flux of $0.63 \pm 0.17 \times 10^4$ m^3 s^{-1}. This additional offshore flux is supplied by the deflected coastal upwelling jet.

In a high-spatial-resolution modeling study around Point Sal, but using upwelling wind events from fall 2015, particles released near the bottom around the point were upwelled into the 20-m-deep, near-surface layer and expelled offshore of Point Sal (Fig. 13; Ahn 2019).

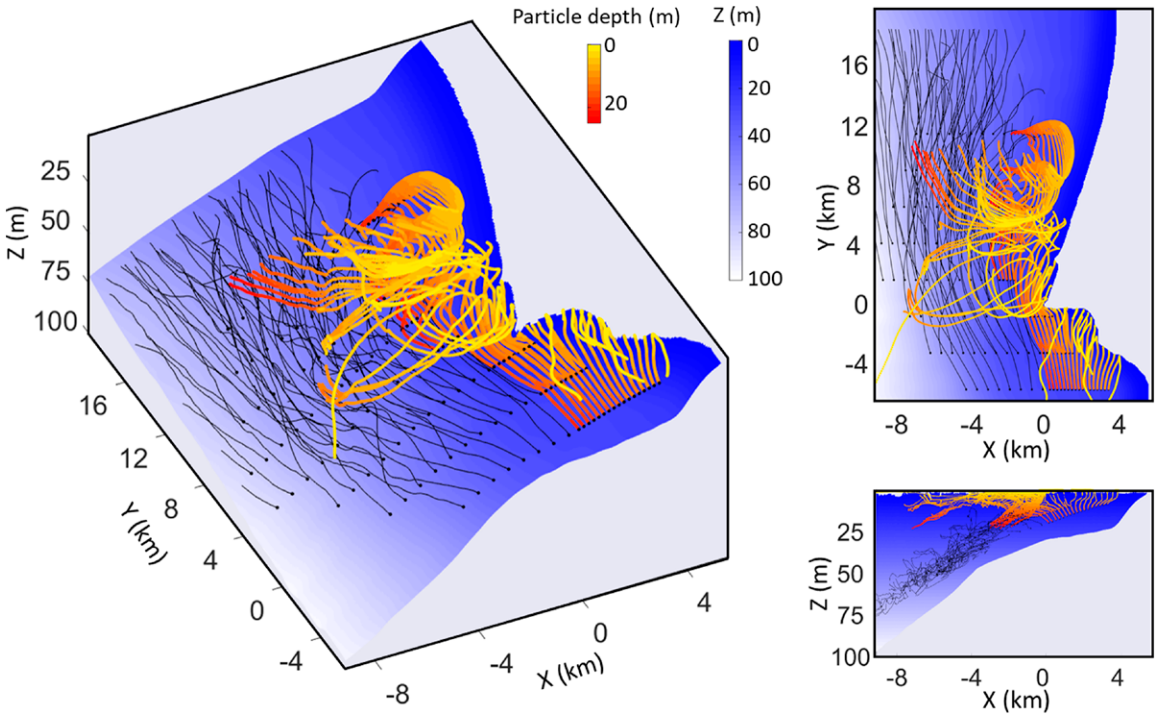

Fig. 13. Lagrangian trajectories for particles launched near the seafloor, at 80% of the water-column depth, along 15 cross sections during an upwelling event in 2015 near Point Sal. Particles launched inshore of the 25 m isobath are colored yellow to red depending on their depth and those released deeper are black. Tracks are shown for 1.5 days (following Ahn 2019).

This model behavior agrees with the moored array and shipboard observations presented in Fig. 12. Furthermore, model studies focused on hindcast of wind relaxation events (Suanda et al. 2016) produce a sharp surface temperature front that propagates northward with the speed of a mixed surface-trapped and slope-controlled buoyancy-driven plume (e.g., Washburn et al. 2011).

Through interaction of the wind- and pressure-driven along-shelf flows around Point Sal, near-surface (20–25 m water depth) water from the inner shelf is fluxed offshore at this coastal promontory. Because this focused offshore flow is also fed by subsurface upwelled water, this flow–topography mechanism is important for expelling upwelled water from the shelf.

Real-time regional wave forecast from directional wave buoys. The 15 directional wave buoys (Fig. 14a) deployed along the 100 m (5 buoys), 50 m (8 buoys), and 20 m isobaths (5 buoys) provided real-time spectral wave information (power spectra and directional moments). This dense array of buoys not only provided detailed wave data at instrumented sites; it also allowed for reconstruction of the regional mean wave field in real time. Specifically, similar to seismic tomography, instrumented sites are related to the incident wave field along a deep-water boundary through backward ray tracing. Following Crosby et al. (2017), observed directional moments at instrumented sites are expressed in terms of the incident directional wave spectrum. The incident spectrum may then be retrieved in the least squares sense from the resulting overdetermined problem. The inverse solution is used as a model boundary in a regular forward wave model (SWAN; Booij et al. 1999) which provides wave conditions throughout the modeled

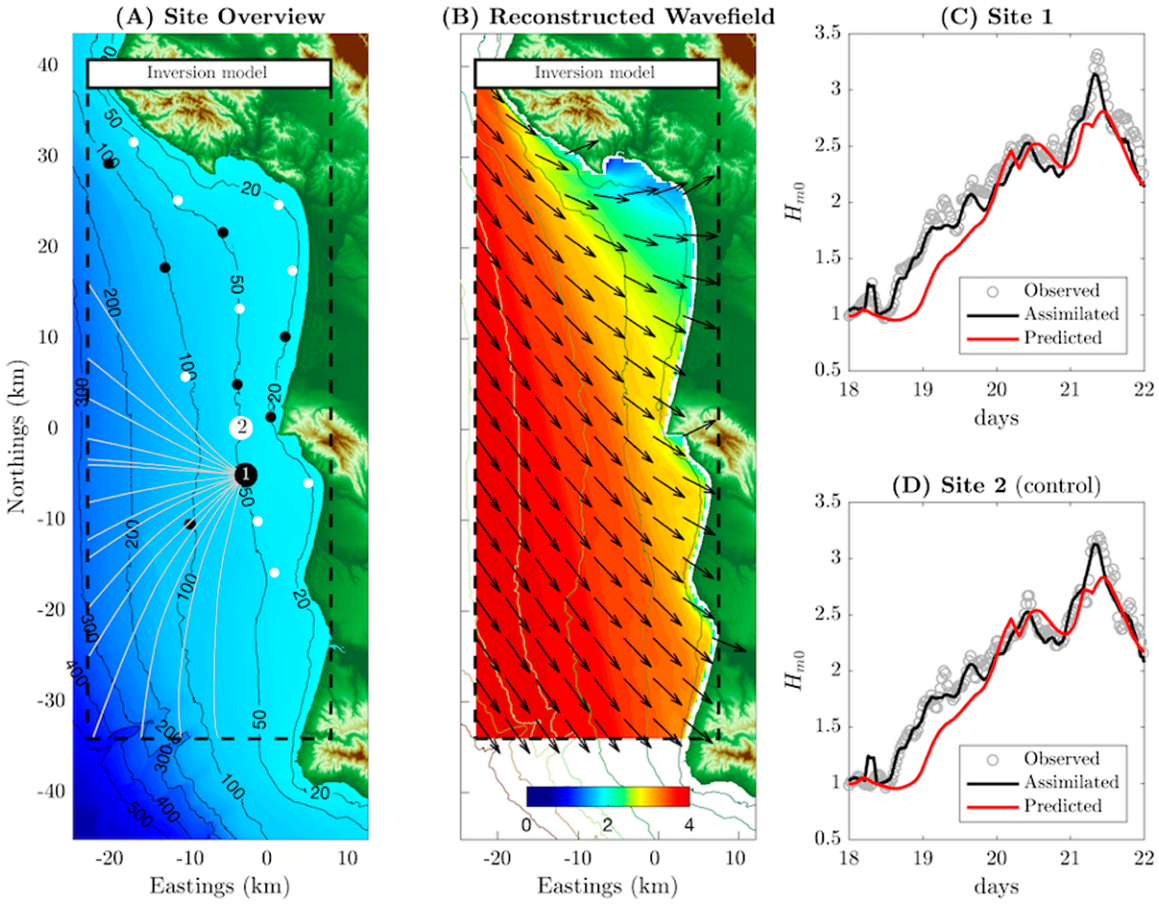

Fig. 14. (a) The buoy array with indicated buoys used in assimilations (black) and those used for control (white). (b) An example reconstruction of significant wave height from the buoys only (no model). Observed significant wave height vs reconstructed and modeled (using WW3 boundary + local SWAN) for (c) a buoy used in assimilation and (d) a control buoy.

region (Fig. 14b). The resulting framework effectively combines spatially separated instruments into a single-directional array that reconstructs the deep-water wave spectrum, from which the regional wave characteristics may be derived. While subject to assumptions such as weak nonlinearity and slow spatial variability of the incident wave field, the fidelity of the reconstructed wave field was typically high, not only at sites included in the inversion procedure (Fig. 14c), but also at control sites not included (Fig. 14d). The coefficient of determination for predicted wave heights at control sites (white markers, Fig. 14a) was 0.95 versus 0.88 for predictions based on NOAA WaveWatch 3 boundary estimates.

Discussion

Detailed in situ and remotely sensed measurements along with numerical model simulations for central California allow for unprecedented investigations into the role of coastal physical processes in creating spatial heterogeneity, and subsequently along-coast variable pathways for cross-shelf exchange in the inner shelf, as discussed here. In addition, questions exploring the interaction between various inner-shelf physical processes are presented.

Spatial heterogeneity. Here we describe ongoing efforts to characterize the spatial heterogeneity of inner-shelf properties through a synthesis of measurements and model results.

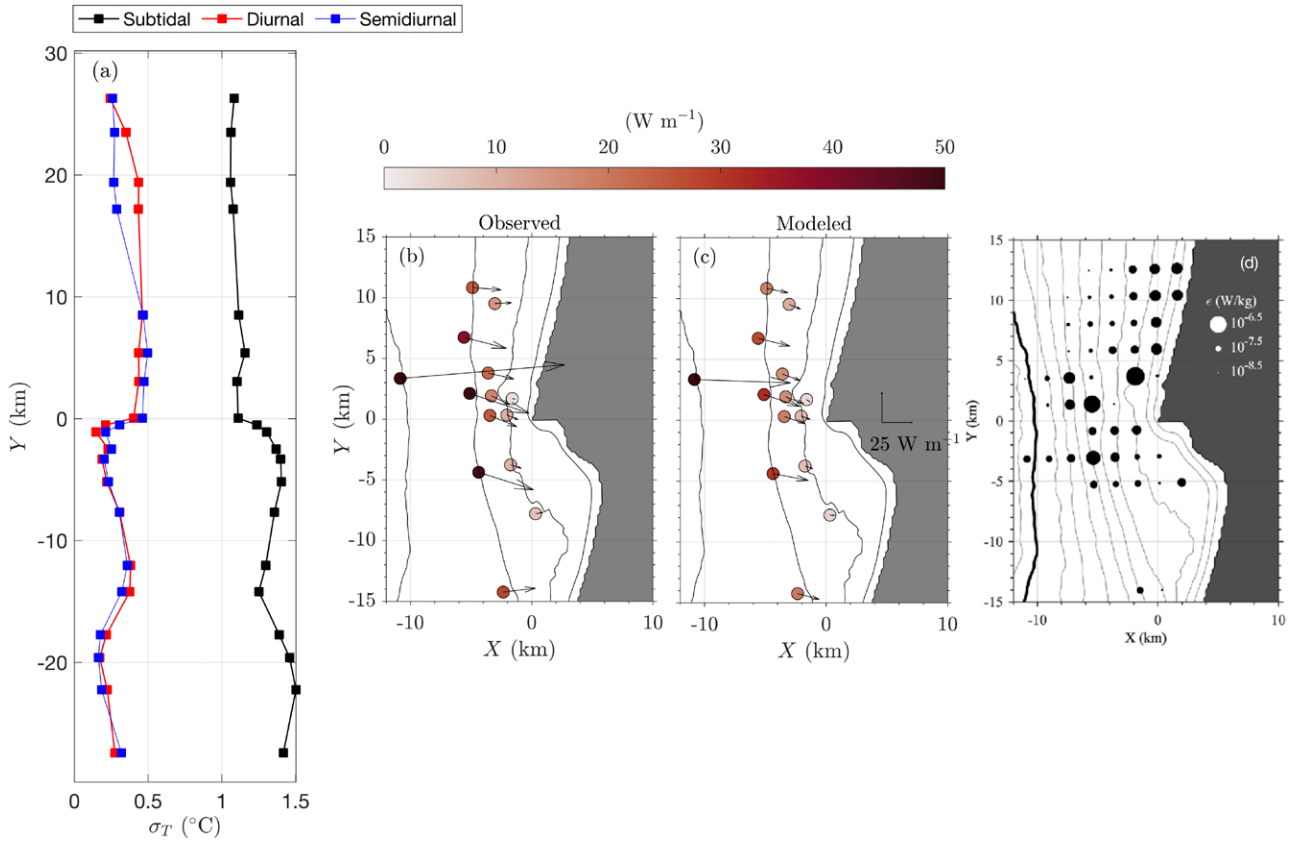

Fig. 15. (a) Standard deviation of mode-one reconstructed EOF subtidal (black), diurnal (red), and semidiurnal (blue) temperature from inner-shelf moorings at water depths of 9–16 m around the Point Sal region (further details are in Feddersen et al. 2020). (b) Observed and (c) modeled depth-integrated, time-averaged semidiurnal internal tidal energy fluxes at water depths of 30–100 m; and (d) depth-averaged dissipation rate (*E*, W kg^{-1}; circles). Color shading in (b) and (c) represents the flux magnitude and the arrows represent the flux vector. Time averaging is over the IOP1. Observations of dissipation rate are obtained from the R/Vs *Sally Ride* and *Oceanus* with the microstructure profiler VMP-250 and a tow-yo'd CTD with a GusT probe attached, respectively. These data were collected over a range of tidal cycles, times, and forcing conditions, and all available vertical profiles are gridded into a 0.02° × 0.02° binned depth-averaged dissipation rate.

An empirical orthogonal function (EOF) analysis of filtered temperature measurements in water depths of 9–16 m (Feddersen et al. 2020) reveals alongshore dependence in temperature variability in subtidal, diurnal, and semidiurnal frequency bands, with Point Sal being a location of strong changes in variability (Fig. 15a). Based on the first EOF mode, subtidal band temperature variability was relatively uniform alongshore with a small gradient just south of Point Sal (black squares, Fig. 15a). Diurnal band variability was high north of Point Sal, and was reduced south of Point Sal and Point Purisima (red squares, Fig. 15b). The EOF analysis reveals southward propagation of the diurnal baroclinic signal (Feddersen et al. 2020). A more comprehensive, ongoing analysis including moorings from 9 to 50 m water depth also shows a consistent diurnal band variability on the length scales of tens of kilometers. Semidiurnal band temperature variability is found to be substantial, especially around the headlands. Variable stratification and Doppler shift associated with eddy activities might lead to this along-shelf inhomogeneity (Kumar et al. 2019; Feddersen et al. 2020).

Spatial heterogeneity of the semidiurnal internal tide signals from the outer to the inner shelf have been investigated using both observations and numerical model simulations (Kumar et al. 2019; Fertitta 2019; McSweeney et al. 2020a). Mean (September 2017) semidiurnal internal tidal energy fluxes at 50 and 30 m isobath are strongest adjacent to Point Sal, decreasing in magnitude both toward the north and south (Figs. 15b,c). The flux magnitude also decreases as internal tides propagate onshore and dissipate, a pattern that is also seen in the mean horizontal kinetic energy (McSweeney et al. 2020a). Furthermore, internal tide properties, such as energy, amplitude, and frontal structure, are influenced by the spatial heterogeneity of stratification (McSweeney et al. 2020a). For example, nonlinear internal bore fronts are found to be alongshore continuous $O(10)$ km at the 50 m isobath and only $O(1)$ km at the 25 m isobath (McSweeney et al. 2020a).

Spatial variability of dissipation rate is quantified using several instruments during the shipboard operations from IOP1 ("Experiment description" section). The distribution of depth-averaged dissipation rate over a portion of the inner shelf with smooth topography (offshore of Oceano) is enhanced in shallower regions decreasing smoothly from onshore to offshore (Fig. 15d). The enhanced dissipation rates in the shallower reaches of the smoother inner shelf may be associated with a variety of processes including surface-layer turbulence by wind and nonlinear internal wave dynamics (Colosi et al. 2018; McSweeney et al. 2020a). Enhanced dissipation occurs at the headlands and complicated bathymetry of Points Sal, Purisima, and Arguello with a more randomly distributed pattern with offshore distance.

Interactions between inner-shelf physical processes. Concurrent measurements of temperature, velocity, turbulence at fixed-mooring locations supplemented by shipboard observations and numerical model results will allow for investigation of the interactions between inner-shelf physical processes. For example, mid- to inner-shelf stratification variability driven by synoptic variations in winds is expected to modify the propagation of semidiurnal internal tides.

X-band radar imagery has suggested periods when nonlinear internal tidal bores interact with offshore-directed rip currents (Fig. 11). The consequences of these interactions on bore propagation, and offshore evolution of rip currents is not known. It is expected that the local change in stratification from advection of water mass within the nonlinear bores will modify the horizontal and vertical extent of rip currents. These interactions have unknown consequences for exchange between the surfzone and the inner shelf, and will be pursued from detailed analysis of observations supplemented by idealized modeling studies.

As previously mentioned, form drag associated with coastline variability influences flow separation, wakes and eddies, and enhanced mixing (Fig. 15d). This is clearly exhibited by a rapid change in diurnal and semidiurnal variability in temperature around headlands (Fig. 15a). It is expected that the momentum transfer from mean flows into eddies and

turbulence will be important to the along-shelf momentum balance. Detailed pressure measurements around Point Sal supplemented by mooring measurements and shipboard observations will facilitate further investigation of this problem. In addition, the eddies shed in the lee of the headland (Fig. 10) may interact with buoyancy fronts in the inner shelf, changing the circulation in thermal wind balance, and inducing ageostrophic secondary circulations (McWilliams 2016).

Finally, the role of turbulence-enhanced mixing of mass and momentum as well as turbulence energy dissipation in controlling the inner-shelf subtidal cross-shelf circulation remains a poorly understood topic. It has been known for a while that changes in vertical mixing as represented by an eddy diffusivity can modify the wind-driven along-shelf and cross-shelf circulations (Lentz 1995b; Lentz et al. 2008). Recent work (Palóczy et al. 2021) has analogously quantified the contribution that turbulent momentum fluxes play in both the cross-shore and alongshore momentum budgets. They find that in both cases the episodic turbulence from passing bores and solitons dominates the long term average of turbulent stresses over diurnal to seasonal time scales. They further find that the turbulent stresses play an order-one role in the cross-shore momentum budget at all depths, pointing to the need for revision of our conceptual model of dynamical balances offshore of the surfzone. Similarly, turbulence at the leading edge of an internal tidal bore may control the propagation (phase speed) and nonlinear evolution of subsequent bores. This question is being explored using mooring and shipboard measurements.

On the regional modeling scale, the hindcast simulations are being used to quantify how modeled subtidal stratification, vertical and horizontal mixing are potentially modified by the addition of barotropic and baroclinic tides (Suanda et al. 2017, 2018). These studies suggest that the addition of remote baroclinic tides reduces the subtidal continental shelf stratification up to 50% relative to simulations without tidal processes. A further analysis using passive particle dispersion in these simulations showed horizontal relative

Nirnimesh Kumar, 1984–2020

Nirnimesh (Nirni) was a coastal physical oceanographer at the University of Washington. He completed his Bachelor of Science in 2007 at the Indian Institute of Technology in West Bengal, India, where he studied ocean engineering and naval architecture. Following that, Nirni completed his M.Sc. and Ph.D. at the University of South Carolina under the supervision of George Voulgaris in 2010 and 2013. Before moving to Seattle, he was a postdoctoral scholar at the Scripps Institution of Oceanography, where he worked on a range of coastal-zone projects including becoming a leader on the ONR-funded Inner-Shelf DRI that this paper describes.

Technically deft and creative, Nirni was blossoming as a leader across a range of research topics. He valued scientific collaboration, the exchange of ideas, and delighted in sharing achievements with others. He had an uncanny ability to develop and maintain collaborations across a wide range of coastal oceanographic regions, from the nearshore of Southern California to the high Arctic polar regions. Nirni was an enthusiastic scientist and an incredibly thoughtful mentor. His gregarious spirit brought an energy to our community that is irreplaceable. He will be remembered for his mischievous smile, his eagerness to help others, his deep scientific insights, and his rigorous work ethic.

This paper is dedicated to our friend, shipmate, and colleague Nirnimesh Kumar. We will miss you more than you can imagine.

Fig. SB1. Nirnimesh Kumar aboard the R/V *Sally Ride* during the Inner-Shelf Dynamics Experiment, 2017.

and vertical dispersion of three-dimensional drifters to be a factor of 2–3 times larger when including baroclinic tides.

Summary

The Inner-Shelf Dynamics Experiment (2015–17) focuses on quantifying the inner-shelf circulation dynamics and stratification evolution caused by a variety of physical processes at work in this region and on understanding and predicting tracer exchange (pollutants, biota, heat) across the inner shelf. The field experiment complemented with numerical model simulations has generated a rich dataset for studying physical processes in the coastal ocean. The highly spatially and temporally resolved oceanographic measurements and numerical simulations of ISDE provides a central framework for studies exploring this complex and fascinating region of the ocean.

Acknowledgments. This work was sponsored by the U.S. Office of Naval Research (ONR) in an ONR Departmental Research Initiative (DRI), Inner-Shelf Dynamics Experiment (ISDE). We thank Dr. Reginald Beach for supporting all the initiatives undertaken as a part of this project. We also thank Colonel Moss, Commander, 30 SW/CC (2017) and Colonel Balts, Commander, 30 SW/CC (2015), Jennifer Tribble, and the operations staff at VAFB for coordinating aircraft access, access to the base, and assisting us in locating and installing our land-based radars. Thanks to the captains and crew members of R/V *Sally Ride*, *Oceanus*, and *Robert Gordon Sproul* for supporting smooth field operations during ISDE. AFW and JAM thank Sam Kelly for the use of his VMP-250. CC and MM thank Dan Clark, Phil Colosimo, Regal Air, Greg Maust, Dave Zucchero, and Bill Retzlaff. JNM and JB thank Pavan Vutukur, Craig Van Appledorn, and Kerry Latham for their contributions to GusT development, testing, construction, and deployment. JAL, JAB, and JMM thank Marnie Jo Zirbel and Taylor Eaton for their contributions to the field work. Bill Boyd, Greg Boyd, Spencer Bull, Tucker Freismuth, Casey Gon, Rob Grenzeback, Ami Hansen, David Honegger, Paul Jessen, Paul Lenz, Aaron Morrone, Andy O'Neill, Lucian Parry, Brett Pickering, Randy Pittman, Greg Sinnett, Kent Smith, Marla Stone, Brian Woodward, and Keith Wyckoff all assisted with the nearshore Point Sal fieldwork. Model simulations were conducted in a high-performance computing machine maintained by Serhad Atakturk and Nick Burmeister and on the Hyak supercomputer system at the University of Washington. JAM, AW and AP thank Paul Chua and Spencer Kawamoto from SIO for their contributions to the *Ride* and *Sproul* research cruises and mooring deployments.

Data availability statement. The movie BAMS-RadarAnimation-IW.mp4 provided in the supplementary information shows the transformation of nonlinear internal waves at high space–time resolution captured by the array of continuously sampling shore-based radars. In situ and remote sensing measurements, along with numerical model solutions are being archived in a repository maintained by the UCSD Library Digital Collections, and also available through National Aeronautics and Space Administration archive.

References

Ahn, S., 2019: Wave energy resource characterization and classification for the United States & numerical simulation of coastal circulation near Point Sal, California. Ph.D. thesis, Georgia Institute of Technology, 192 pp.

Allen, J. S., and Coauthors, 1983: Physical oceanography of continental shelves. *Rev. Geophys.*, **21**, 1149–1181, https://doi.org/10.1029/RG021i005p01149.

Allen, R. M., J. A. Simeonov, J. Calantoni, M. T. Stacey, and E. A. Variano, 2018: Turbulence in the presence of internal waves in the bottom boundary layer of the California inner shelf. *Ocean Dyn.*, **68**, 627–644, https://doi.org/10.1007/s10236-018-1147-7.

Aristizábal, M. F., M. R. Fewings, and L. Washburn, 2017: Effects of the relaxation of upwelling-favorable winds on the diurnal and semidiurnal water temperature fluctuations in the Santa Barbara channel, California. *J. Geophys. Res. Oceans*, **122**, 7958–7977, https://doi.org/10.1002/2017JC013199.

Auad, G., M. C. Hendershott, and C. D. Winant, 1998: Wind-induced currents and bottom-trapped waves in the Santa Barbara channel. *J. Phys. Oceanogr.*, **28**, 85–102, https://doi.org/10.1175/1520-0485(1998)028<0085:WICABT>2.0.CO;2.

Austin, J. A., and S. J. Lentz, 2002: The inner shelf response to wind-driven upwelling and downwelling. *J. Phys. Oceanogr.*, **32**, 2171–2193, https://doi.org/10.1175/1520-0485(2002)032<2171:TISRTW>2.0.CO;2.

Austin, M. J., T. M. Scott, P. E. Russell, and G. Masselink, 2013: Rip current prediction: Development, validation, and evaluation of an operational tool. *J. Coastal Res.*, **29**, 283–300, https://doi.org/10.2112/JCOASTRES-D-12-00093.1.

Bassin, C. J., L. Washburn, M. Brzezinski, and E. McPhee-Shaw, 2005: Submesoscale coastal eddies observed by high frequency radar: A new mechanism for delivering nutrients to kelp forests in the southern California Bight. *Geophys. Res. Lett.*, **32**, L12604, https://doi.org/10.1029/2005GL023017.

Beardsley, R., and S. Lentz, 1987: The coastal ocean dynamics experiment collection: An introduction. *J. Geophys. Res.*, **92**, 1455–1463, https://doi.org/10.1029/JC092iC02p01455.

Becherer, J., J. N. Moum, J. A. Colosi, J. A. Lerczak, and J. M. McSweeney, 2020: Turbulence asymmetries in bottom boundary layer velocity pulses associated with onshore-propagating nonlinear internal waves. *J. Phys. Oceanogr.*, **50**, 2373–2391, https://doi.org/10.1175/JPO-D-19-0178.1.

——, and Coauthors, 2021a: Saturation of the internal tide over the inner continental shelf. Part I: Observations. *J. Phys. Oceanogr.*, https://doi.org/10.1175/JPO-D-20-0264.1, in press.

——, and Coauthors, 2021b: Saturation of the internal tide over the inner continental shelf. Part II: Parameterization. *J. Phys. Oceanogr.*, in press.

Boehm, A. B., N. S. Ismail, L. M. Sassoubre, and E. A. Andruszkiewicz, 2017: Oceans in peril: Grand challenges in applied water quality research for the 21st century. *Environ. Eng. Sci.*, **34**, 3–15, https://doi.org/10.1089/ees.2015.0252.

Booij, N., R. C. Ris, and L. H. Holthuijsen, 1999: A third-generation wave model for coastal regions: 1. Model description and validation. *J. Geophys. Res.*, **104**, 7649–7666, https://doi.org/10.1029/98JC02622.

Bourgault, D., D. E. Kelley, and P. S. Galbraith, 2008: Turbulence and boluses on an internal beach. *J. Mar. Res.*, **66**, 563–588, https://doi.org/10.1357/002224008787536835.

Bruneau, N., P. Bonneton, B. Castelle, and R. Pedreros, 2011: Modeling rip current circulations and vorticity in a high-energy mesotidal-macrotidal environment. *J. Geophys. Res.*, **116**, C07026, https://doi.org/10.1029/2010JC006693.

Butman, B., P. S. Alexander, A. Scotti, R. C. Beardsley, and S. P. Anderson, 2006: Large internal waves in Massachusetts Bay transport sediments offshore. *Cont. Shelf Res.*, **26**, 2029–2049, https://doi.org/10.1016/j.csr.2006.07.022.

Butman, C., 1994: CoOP: Coastal Ocean Processes study interdisciplinary approach, new technology to determine coupled biological, physical, geological processes affecting larval transport on inner shelf. *Sea Technol.*, **50**, 44–49.

Cairns, J., 1967: Asymmetry of internal tidal waves in shallow coastal waters. *J. Geophys. Res.*, **72**, 3563–3565, https://doi.org/10.1029/JZ072i014p03563.

Callendar, W., J. Klymak, and M. Foreman, 2011: Tidal generation of large sub-mesoscale eddy dipoles. *Ocean Sci.*, **7**, 487–502, https://doi.org/10.5194/os-7-487-2011.

Canals, M., G. Pawlak, and P. MacCready, 2009: Tilted baroclinic tidal vortices. *J. Phys. Oceanogr.*, **39**, 333–350, https://doi.org/10.1175/2008JPO3954.1.

Capet, X., J. C. McWilliams, M. J. Molemaker, and A. Shchepetkin, 2008: Mesoscale to submesoscale transition in the California Current System. Part I: Flow structure, eddy flux, and observational tests. *J. Phys. Oceanogr.*, **38**, 29–43, https://doi.org/10.1175/2007JPO3671.1.

Castelle, B., T. Scott, R. Brander, and R. McCarroll, 2016: Rip current types, circulation and hazard. *Earth-Sci. Rev.*, **163**, 1–21, https://doi.org/10.1016/j.earscirev.2016.09.008.

Celona, S., S. T. Merrifield, T. de Paolo, N. Kaslan, T. Cook, E. J. Terrill, and J. A. Colosi, 2021: Automated Detection, Classification, and Tracking of Internal Wave Signatures Using X-Band Radar in the Inner Shelf. *J. Atmos. Oceanic Technol.*, **38**, 789–803, https://journals.ametsoc.org/view/journals/atot/38/4/JTECH-D-20-0129.1.xml.

Clark, D. B., S. Elgar, and B. Raubenheimer, 2012: Vorticity generation by short-crested wave breaking. *Geophys. Res. Lett.*, **39**, L24604, https://doi.org/10.1029/2012GL054034.

Colosi, J. A., N. Kumar, S. H. Suanda, T. M. Freismuth, and J. H. MacMahan, 2018: Statistics of internal tide bores and internal solitary waves observed on the inner continental shelf off Point Sal, California. *J. Phys. Oceanogr.*, **48**, 123–143, https://doi.org/10.1175/JPO-D-17-0045.1.

Crosby, S. C., B. D. Cornuelle, W. C. O'Reilly, and R. T. Guza, 2017: Assimilating global wave model predictions and deep-water wave observations in nearshore swell predictions. *J. Atmos. Oceanic Technol.*, **34**, 1823–1836, https://doi.org/10.1175/JTECH-D-17-0003.1.

Cudaback, C. N., and E. McPhee-Shaw, 2009: Diurnal-period internal waves near Point Conception, California. *Estuarine Coastal Shelf Sci.*, **83**, 349–359, https://doi.org/10.1016/j.ecss.2008.12.018.

——, L. Washburn, and E. Dever, 2005: Subtidal inner-shelf circulation near Point Conception, California. *J. Geophys. Res.*, **110**, C10007, https://doi.org/10.1029/2004JC002608.

Dalrymple, R. A., J. H. MacMahan, A. J. Reniers, and V. Nelko, 2011: Rip currents. *Annu. Rev. Fluid Mech.*, **43**, 551–581, https://doi.org/10.1146/annurev-fluid-122109-160733.

Dauhajre, D. P., J. C. McWilliams, and L. Renault, 2019: Nearshore Lagrangian connectivity: Submesoscale influence and resolution sensitivity. *J. Geophys. Res. Oceans*, **124**, 5180–5204, https://doi.org/10.1029/2019JC014943.

Dewar, W., J. McWilliams, and M. Molemaker, 2015: Centrifugal instability and mixing in the California Undercurrent. *J. Phys. Oceanogr.*, **45**, 1224–1241, https://doi.org/10.1175/JPO-D-13-0269.1.

Doglioli, A. M., A. Griffa, and M. G. Magaldi, 2004: Numerical study of a coastal current on a steep slope in presence of a cape: The case of the Promontorio di Portofino. *J. Geophys. Res.*, **109**, C12033, https://doi.org/10.1029/2004JC002422.

Dorman, C., and C. Winant, 2000: The structure and variability of the marine atmosphere around the Santa Barbara Channel. *Mon. Wea. Rev.*, **128**, 261–282, https://doi.org/10.1175/1520-0493(2000)128<0261:TSAVOT>2.0.CO;2.

Doyle, J. D., Q. Jiang, Y. Chao, and J. Farrara, 2009: High-resolution real-time modeling of the marine atmospheric boundary layer in support of the AOSN-II field campaign. *Deep-Sea Res. II*, **56**, 87–99, https://doi.org/10.1016/j.dsr2.2008.08.009.

Feddersen, F., 2014: The generation of surfzone eddies in a strong alongshore current. *J. Phys. Oceanogr.*, **44**, 600–617, https://doi.org/10.1175/JPO-D-13-051.1.

——, J. H. MacMahan, T. M. Freismuth, M. K. Gough, and M. Kovatch, 2020: Inner-shelf vertical and alongshore temperature variability in the subtidal, diurnal, and semidiurnal bands along the central California coastline with headlands. *J. Geophys. Res. Oceans*, **125**, e2019JC015347, https://doi.org/10.1029/2019JC015347.

Fertitta, D. A., 2019: Semidiurnal internal tides in the Santa Maria basin. M.S. thesis, University of Washington, 73 pp.

Fewings, M. R., and S. J. Lentz, 2010: Momentum balances on the inner continental shelf at Martha's Vineyard Coastal Observatory. *J. Geophys. Res.*, **115**, C12023, https://doi.org/10.1029/2009JC005578.

——, and ——, 2011: Summertime cooling of the shallow continental shelf. *J. Geophys. Res.*, **116**, C07015, https://doi.org/10.1029/2010JC006744.

——, ——, and J. Fredericks, 2008: Observations of cross-shelf flow driven by cross-shelf winds on the inner continental shelf. *J. Phys. Oceanogr.*, **38**, 2358–2378, https://doi.org/10.1175/2008JPO3990.1.

——, L. Washburn, and J. C. Ohlmann, 2015: Coastal water circulation patterns around the northern Channel Islands and Point Conception, California. *Prog. Oceanogr.*, **138**, 283–304, https://doi.org/10.1016/j.pocean.2015.10.001.

Garvine, R. W., 2004: The vertical structure and subtidal dynamics of the inner shelf off New Jersey. *J. Mar. Res.*, **62**, 337–371, https://doi.org/10.1357/0022240041446182.

Giddings, S. N., and Coauthors, 2014: Hindcasts of potential harmful algal bloom transport pathways on the Pacific Northwest coast. *J. Geophys. Res. Oceans*, **119**, 2439–2461, https://doi.org/10.1002/2013JC009622.

Gove, J. M., and Coauthors, 2016: Near-island biological hotspots in barren ocean basins. *Nat. Commun.*, **7**, 10581, https://doi.org/10.1038/ncomms10581.

Grant, S. B., J. H. Kim, B. H. Jones, S. A. Jenkins, J. Wasyl, and C. Cudaback, 2005: Surf zone entrainment, along-shore transport, and human health implications of pollution from tidal outlets. *J. Geophys. Res.*, **110**, C10025, https://doi.org/10.1029/2004JC002401.

Grimes, D. J., F. Feddersen, and N. Kumar, 2020a: Tracer exchange across the stratified inner-shelf driven by transient rip-currents and diurnal surface heat fluxes. *Geophys. Res. Lett.*, **47**, e2019GL086501, https://doi.org/10.1029/2019GL086501.

——, ——, S. N. Giddings, and G. Pawlak, 2020b: Cross-shore deformation of a surfzone-released dye plume by an internal tide on the inner shelf. *J. Phys. Oceanogr.*, **50**, 35–54, https://doi.org/10.1175/JPO-D-19-0046.1.

Guerra, M., and J. Thomson, 2017: Turbulence measurements from five-beam acoustic Doppler current profilers. *J. Atmos. Oceanic Technol.*, **34**, 1267–1284, https://doi.org/10.1175/JTECH-D-16-0148.1.

Gula, J., M. J. Molemaker, and J. C. McWilliams, 2016a: Submesoscale dynamics of a Gulf Stream frontal eddy in the South Atlantic Bight. *J. Phys. Oceanogr.*, **46**, 305–325, https://doi.org/10.1175/JPO-D-14-0258.1.

——, ——, and ——, 2016b: Topographic generation of submesoscale centrifugal instability and energy dissipation. *Nat. Commun.*, **7**, 12811, https://doi.org/10.1038/ncomms12811.

Haller, M. C., R. A. Dalrymple, and I. A. Svendsen, 2002: Experimental study of nearshore dynamics on a barred beach with rip channels. *J. Geophys. Res.*, **107**, 3061, https://doi.org/10.1029/2001JC000955.

——, D. Honegger, and P. A. Catalan, 2014: Rip current observations via marine radar. *J. Waterw. Port Coastal Ocean Eng.*, **140**, 115–124, https://doi.org/10.1061/(ASCE)WW.1943-5460.0000229.

Hally-Rosendahl, K., and F. Feddersen, 2016: Modeling surfzone to inner-shelf tracer exchange. *J. Geophys. Res. Oceans*, **121**, 4007–4025, https://doi.org/10.1002/2015JC011530.

——, ——, and R. Guza, 2014: Cross-shore tracer exchange between the surfzone and inner-shelf. *J. Geophys. Res. Oceans*, **119**, 4367–4388, https://doi.org/10.1002/2013JC009722.

——, ——, D. B. Clark, and R. Guza, 2015: Surfzone to inner-shelf exchange estimated from dye tracer balances. *J. Geophys. Res. Oceans*, **120**, 6289–6308, https://doi.org/10.1002/2015JC010844.

Hickey, B., E. Dobbins, and S. E. Allen, 2003: Local and remote forcing of currents and temperature in the central Southern California Bight. *J. Geophys. Res.*, **108**, 3081, https://doi.org/10.1029/2000JC000313.

Hodur, R. M., X. Hong, J. D. Doyle, J. Pullen, J. Cummings, P. Martin, and M. A. Rennick, 2002: The Coupled Ocean/Atmosphere Mesoscale Prediction System (COAMPS). *Oceanography*, **15** (1), 88–98, https://doi.org/10.5670/oceanog.2002.39.

Horwitz, R., and S. J. Lentz, 2014: Inner-shelf response to cross-shelf wind stress: The importance of the cross-shelf density gradient in an idealized numerical model and field observations. *J. Phys. Oceanogr.*, **44**, 86–103, https://doi.org/10.1175/JPO-D-13-075.1.

——, and ——, 2016: The effect of wind direction on cross-shelf transport on an initially stratified inner shelf. *J. Mar. Res.*, **74**, 201–227, https://doi.org/10.1357/002224016820870648.

Huyer, A., and P. M. Kosro, 1987: Mesoscale surveys over the shelf and slope in the upwelling region near Point Arena, California. *J. Geophys. Res.*, **92**, 1655–1681, https://doi.org/10.1029/JC092iC02p01655.

Jones, O., R. Simons, E. Jones, and J. Harris, 2006: Influence of seabed slope and Coriolis effects on the development of sandbanks near headlands. *J. Geophys. Res.*, **111**, C03020, https://doi.org/10.1029/2005JC002944.

Karnauskas, M., L. M. Chérubin, and C. B. Paris, 2011: Adaptive significance of the formation of multi-species fish spawning aggregations near submerged capes. *PLOS ONE*, **6**, e22067, https://doi.org/10.1371/journal.pone.0022067.

Kirincich, A., 2016: The occurrence, drivers, and implications of submesoscale eddies on the Martha's Vineyard inner shelf. *J. Phys. Oceanogr.*, **46**, 2645–2662, https://doi.org/10.1175/JPO-D-15-0191.1.

——, and S. Lentz, 2017: The importance of lateral variability on exchange across the inner shelf south of Martha's Vineyard, MA. *J. Geophys. Res. Oceans*, **122**, 2360–2381, https://doi.org/10.1002/2016JC012491.

——, J. A. Barth, B. A. Grantham, B. A. Menge, and J. Lubchenco, 2005: Wind-driven inner-shelf circulation off central Oregon during summer. *J. Geophys. Res.*, **110**, C10S03, https://doi.org/10.1029/2004JC002611.

——, S. J. Lentz, J. T. Farrar, and N. K. Ganju, 2013: The spatial structure of tidal and mean circulation over the inner shelf south of Martha's Vineyard, Massachusetts. *J. Phys. Oceanogr.*, **43**, 1940–1958, https://doi.org/10.1175/JPO-D-13-020.1.

Kovatch, F. F. M., F. Feddersen, D. G. Grimes, and J. H. MacMahan, 2021: Vorticity recirculation and asymmetric generation at a small headland with broadband currents. *J. Geophys. Res. Oceans*, **126**, e2020JC016639, https://doi.org/10.1029/2020JC016639.

Kumar, N., and F. Feddersen, 2017a: A new offshore transport mechanism for shoreline-released tracer induced by transient rip currents and stratification. *Geophys. Res. Lett.*, **44**, 2843–2851, https://doi.org/10.1002/2017GL072611.

——, and ——, 2017b: The effect of Stokes drift and transient rip currents on the inner shelf. Part I: No stratification. *J. Phys. Oceanogr.*, **47**, 227–241, https://doi.org/10.1175/JPO-D-16-0076.1.

——, and ——, 2017c: The effect of Stokes drift and transient rip currents on the inner shelf. Part II: With stratification. *J. Phys. Oceanogr.*, **47**, 243–260, https://doi.org/10.1175/JPO-D-16-0077.1.

——, G. Voulgaris, J. C. Warner, and M. Olabarrieta, 2012: Implementation of the vortex force formalism in the Coupled Ocean-Atmosphere-Wave-Sediment Transport (COAWST) modeling system for inner shelf and surf zone applications. *Ocean Modell.*, **47**, 65–95, https://doi.org/10.1016/j.ocemod.2012.01.003.

——, F. Feddersen, Y. Uchiyama, J. McWilliams, and W. O'Reilly, 2015: Midshelf to surfzone coupled ROMS–SWAN model data comparison of waves, currents, and temperature: Diagnosis of subtidal forcings and response. *J. Phys. Oceanogr.*, **45**, 1464–1490, https://doi.org/10.1175/JPO-D-14-0151.1.

——, ——, S. Suanda, Y. Uchiyama, and J. McWilliams, 2016: Mid- to inner-shelf coupled ROMS–SWAN model–data comparison of currents and temperature: Diurnal and semidiurnal variability. *J. Phys. Oceanogr.*, **46**, 841–862, https://doi.org/10.1175/JPO-D-15-0103.1.

——, S. H. Suanda, J. A. Colosi, K. Haas, E. Di Lorenzo, A. J. Miller, and C. A. Edwards, 2019: Coastal semidiurnal internal tidal incoherence in the Santa Maria basin, California: Observations and model simulations. *J. Geophys. Res. Oceans*, **124**, 5158–5179, https://doi.org/10.1029/2018JC014891.

Lee, O. S., 1961: Observations on internal waves in shallow water. *Limnol. Oceanogr.*, **6**, 312–321, https://doi.org/10.4319/lo.1961.6.3.0312.

Leichter, J. J., G. Shellenbarger, S. J. Genovese, and S. R. Wing, 1998: Breaking internal waves on a Florida (USA) coral reef: A plankton pump at work? *Mar. Ecol. Prog. Ser.*, **166**, 83–97, https://doi.org/10.3354/meps166083.

Lenain, L., and W. K. Melville, 2017: Measurements of the directional spectrum across the equilibrium saturation ranges of wind-generated surface waves. *J. Phys. Oceanogr.*, **47**, 2123–2138, https://doi.org/10.1175/JPO-D-17-0017.1.

——, N. M. Statom, and W. K. Melville, 2019: Airborne measurements of surface wind and slope statistics over the ocean. *J. Phys. Oceanogr.*, **49**, 2799–2814, https://doi.org/10.1175/JPO-D-19-0098.1.

Lennert-Cody, C. E., and P. J. Franks, 1999: Plankton patchiness in high-frequency internal waves. *Mar. Ecol. Prog. Ser.*, **186**, 59–66, https://doi.org/10.3354/meps186059.

Lentz, S. J., 1994: Current dynamics over the Northern California inner shelf. *J. Phys. Oceanogr.*, **24**, 2461–2478, https://doi.org/10.1175/1520-0485(1994)024<2461:CDOTNC>2.0.CO;2.

——, 1995a: U.S. contributions to the physical oceanography of continental shelves in the early 1990's. *Rev. Geophys.*, **33**, 1225–1236, https://doi.org/10.1029/95RG00177.

——, 1995b: Sensitivity of the inner-shelf circulation to the form of the eddy viscosity profile. *J. Phys. Oceanogr.*, **25**, 19–28, https://doi.org/10.1175/1520-0485(1995)025<0019:SOTISC>2.0.CO;2.

——, and M. R. Fewings, 2012: The wind- and wave-driven inner-shelf circulation. *Annu. Rev. Mar. Sci.*, **4**, 317–343, https://doi.org/10.1146/annurev-marine-120709-142745.

——, R. Guza, S. Elgar, F. Feddersen, and T. Herbers, 1999: Momentum balances on the North Carolina inner shelf. *J. Geophys. Res.*, **104**, 18 205–18 226, https://doi.org/10.1029/1999JC900101.

——, M. Fewings, P. Howd, J. Fredericks, and K. Hathaway, 2008: Observations and a model of undertow over the inner continental shelf. *J. Phys. Oceanogr.*, **38**, 2341–2357, https://doi.org/10.1175/2008JPO3986.1.

Lerczak, J. A., C. Winant, and M. Hendershott, 2003: Observations of the semidiurnal internal tide on the southern California slope and shelf. *J. Geophys. Res.*, **108**, 3068, https://doi.org/10.1029/2001JC001128.

Long, J. W., and H. T. Özkan-Haller, 2009: Low-frequency characteristics of wave group–forced vortices. *J. Geophys. Res.*, **114**, C08004, https://doi.org/10.1029/2008JC004894.

MacKinnon, J. A., M. H. Alford, G. Voet, K. L. Zeiden, T. Shaun Johnston, M. Siegelman, S. Merrifield, and M. Merrifield, 2019: Eddy wake generation from broadband currents near Palau. *J. Geophys. Res. Oceans*, **124**, 4891–4903, https://doi.org/10.1029/2019JC014945.

MacMahan, J. H., E. B. Thornton, and A. J. Reniers, 2006: Rip current review. *Coastal Eng.*, **53**, 191–208, https://doi.org/10.1016/j.coastaleng.2005.10.009.

——, and Coauthors, 2010: Mean Lagrangian flow behavior on an open coast rip-channeled beach: A new perspective. *Mar. Geol.*, **268**, 1–15, https://doi.org/10.1016/j.margeo.2009.09.011.

Mark, D. J., E. A. Spargo, J. J. Westerink, and R. A. Luettich Jr., 2004: ENPAC 2003: A tidal constituent database for eastern North Pacific Ocean. U.S. Army Engineer Research and Development Center Tech. Rep., 191 pp.

Marmorino, G. O., G. B. Smith, and W. D. Miller, 2013: Infrared remote sensing of surf-zone eddies. *IEEE J. Sel. Top. Appl. Earth Obs. Remote Sens.*, **6**, 1710–1718, https://doi.org/10.1109/JSTARS.2013.2257695.

Mazzini, P. L., J. A. Barth, R. K. Shearman, and A. Erofeev, 2014: Buoyancy-driven coastal currents off Oregon during fall and winter. *J. Phys. Oceanogr.*, **44**, 2854–2876, https://doi.org/10.1175/JPO-D-14-0012.1.

McSweeney, J. M., and Coauthors, 2020a: Alongshore variability of shoaling internal bores on the inner shelf. *J. Phys. Oceanogr.*, **50**, 2965–2981, https://doi.org/10.1175/JPO-D-20-0090.1.

——, and Coauthors, 2020b: Observations of shoaling nonlinear internal bores across the central California inner shelf. *J. Phys. Oceanogr.*, **50**, 111–132, https://doi.org/10.1175/JPO-D-19-0125.1.

McWilliams, J. C., 2016: Submesoscale currents in the ocean. *Proc. Roy. Soc.*, **472A**, 20160117, https://doi.org/10.1098/rspa.2016.0117.

Melton, C., L. Washburn, and C. Gotschalk, 2009: Wind relaxations and poleward flow events in a coastal upwelling system on the central California coast. *J. Geophys. Res.*, **114**, C11016, https://doi.org/10.1029/2009JC005397.

Melville, W. K., L. Lenain, D. R. Cayan, M. Kahru, J. P. Kleissl, P. F. Linden, and N. M. Statom, 2016: The Modular Aerial Sensing System. *J. Atmos. Oceanic Technol.*, **33**, 1169–1184, https://doi.org/10.1175/JTECH-D-15-0067.1.

Mitchum, G. T., and A. J. Clarke, 1986: The frictional nearshore response to forcing by synoptic scale winds. *J. Phys. Oceanogr.*, **16**, 934–946, https://doi.org/10.1175/1520-0485(1986)016<0934:TFNRTF>2.0.CO;2.

Molina, L., G. Pawlak, J. Wells, S. Monismith, and M. Merrifield, 2014: Diurnal cross-shore thermal exchange on a tropical forereef. *J. Geophys. Res. Oceans*, **119**, 6101–6120, https://doi.org/10.1002/2013JC009621.

Moulton, M., S. Elgar, B. Raubenheimer, J. C. Warner, and N. Kumar, 2017: Rip currents and alongshore flows in single channels dredged in the surf zone. *J. Geophys. Res. Oceans*, **122**, 3799–3816, https://doi.org/10.1002/2016JC012222.

——, C. C. Chickadel, and J. Thomson, 2021: Warm and cool nearshore plumes connecting the surf zone to the inner shelf. *Geophys. Res. Lett.*, e2020GL091675, https://doi.org/10.1029/2020GL091675, in press.

Moum, J., and J. Nash, 2008: Seafloor pressure measurements of nonlinear internal waves. *J. Phys. Oceanogr.*, **38**, 481–491, https://doi.org/10.1175/2007JPO3736.1.

——, and ——, 2009: Mixing measurements on an equatorial ocean mooring. *J. Atmos. Oceanic Technol.*, **26**, 317–336, https://doi.org/10.1175/2008JTECHO617.1.

Nidzieko, N., and J. Largier, 2013: Inner shelf intrusions of offshore water in an upwelling system affect coastal connectivity. *Geophys. Res. Lett.*, **40**, 5423–5428, https://doi.org/10.1002/2013GL056756.

Noyes, T. J., R. Guza, S. Elgar, and T. Herbers, 2004: Field observations of shear waves in the surf zone. *J. Geophys. Res.*, **109**, C01031, https://doi.org/10.1029/2002JC001761.

O'Dea, A., N. Kumar, and M. Haller, 2021: Simulations of the surf zone eddy field and cross-shore exchange on a non-idealized bathymetry. *J. Geophys. Res. Oceans*, **126**, e2020JC016619, https://doi.org/10.1029/2020JC016619.

Olabarrieta, M., J. C. Warner, and N. Kumar, 2011: Wave-current interaction in Willapa Bay. *J. Geophys. Res.*, **116**, C12014, https://doi.org/10.1029/2011JC007387.

Özkan-Haller, H. T., and J. T. Kirby, 1999: Nonlinear evolution of shear instabilities of the longshore current: A comparison of observations and computations. *J. Geophys. Res.*, **104**, 25 953–25 984, https://doi.org/10.1029/1999JC900104.

Palóczy, A., J. MacKinnon, and A. Waterhouse, 2021: Subtidal to supertidal variability of Reynolds stresses in a mid-latitude stratified inner-shelf. *J. Phys. Oceanogr.*, **51**, 1091–1111, https://doi.org/10.1175/JPO-D-20-0140.1.

Pawlak, G., and P. MacCready, 2002: Oscillatory flow across an irregular boundary. *J. Geophys. Res.*, **107**, 3036, https://doi.org/10.1029/2000JC000596.

——, ——, K. A. Edwards, and R. McCabe, 2003: Observations on the evolution of tidal vorticity at a stratified deep water headland. *Geophys. Res. Lett.*, **30**, 2234–2237, https://doi.org/10.1029/2003GL018092.

Peregrine, D., 1998: Surf zone currents. *Theor. Comput. Fluid Dyn.*, **10**, 295–309, https://doi.org/10.1007/s001620050065.

Pineda, J., 1991: Predictable upwelling and the shoreward transport of planktonic larvae by internal tidal bores. *Science*, **253**, 548–549, https://doi.org/10.1126/science.253.5019.548.

Raghukumar, K., G. Chang, F. Spada, C. Jones, T. Janssen, and A. Gans, 2019: Performance characteristics of "Spotter," a newly developed real-time wave measurement buoy. *J. Atmos. Oceanic Technol.*, **36**, 1127–1141, https://doi.org/10.1175/JTECH-D-18-0151.1.

Roughan, M., A. J. Mace, J. L. Largier, S. G. Morgan, J. L. Fisher, and M. L. Carter, 2005: Subsurface recirculation and larval retention in the lee of a small headland: A variation on the upwelling shadow theme. *J. Geophys. Res.*, **110**, C10027, https://doi.org/10.1029/2005JC002898.

Scannell, B. D., T. P. Rippeth, J. H. Simpson, J. A. Polton, and J. E. Hopkins, 2017: Correcting surface wave bias in structure function estimates of turbulent kinetic energy dissipation rate. *J. Atmos. Oceanic Technol.*, **34**, 2257–2273, https://doi.org/10.1175/JTECH-D-17-0059.1.

Scotti, A., and J. Pineda, 2004: Observation of very large and steep internal waves of elevation near the Massachusetts coast. *Geophys. Res. Lett.*, **31**, L22307, https://doi.org/10.1029/2004GL021052.

Shanks, A. L., and W. G. Wright, 1987: Internal-wave-mediated shoreward transport of cyprids, megalopae, and gammarids and correlated longshore differences in the settling rate of intertidal barnacles. *J. Exp. Mar. Biol. Ecol.*, **114**, 1–13, https://doi.org/10.1016/0022-0981(87)90135-3.

Shchepetkin, A. F., and J. C. McWilliams, 2005: The Regional Oceanic Modeling System (ROMS): A split-explicit, free-surface, topography-following-coordinate oceanic model. *Ocean Modell.*, **9**, 347–404, https://doi.org/10.1016/j.ocemod.2004.08.002.

——, and ——, 2009: Correction and commentary for "Ocean forecasting in terrain-following coordinates: Formulation and skill assessment of the regional ocean modeling system" by Haidvogel et al., J. Comp. Phys. 227, pp. 3595–3624. *J. Comput. Phys.*, **228**, 8985–9000, https://doi.org/10.1016/j.jcp.2009.09.002.

Shroyer, E., J. Moum, and J. Nash, 2010: Vertical heat flux and lateral mass transport in nonlinear internal waves. *Geophys. Res. Lett.*, **37**, L08601, https://doi.org/10.1029/2010GL042715.

Signell, R. P., and W. R. Geyer, 1991: Transient eddy formation around headlands. *J. Geophys. Res.*, **96**, 2561–2575, https://doi.org/10.1029/90JC02029.

Sinnett, G., and F. Feddersen, 2019: The nearshore heat budget: Effects of stratification and surfzone dynamics. *J. Geophys. Res. Oceans*, **124**, 8219–8240, https://doi.org/10.1029/2019JC015494.

——, ——, A. J. Lucas, G. Pawlak, and E. Terrill, 2018: Observations of nonlinear internal wave run-up to the surfzone. *J. Phys. Oceanogr.*, **48**, 531–554, https://doi.org/10.1175/JPO-D-17-0210.1.

Spydell, M., and F. Feddersen, 2009: Lagrangian drifter dispersion in the surf zone: Directionally spread, normally incident waves. *J. Phys. Oceanogr.*, **39**, 809–830, https://doi.org/10.1175/2008JPO3892.1.

——, ——, and J. Macmahan, 2019: The effect of drifter GPS errors on estimates of submesoscale vorticity. *J. Atmos. Oceanic Technol.*, **36**, 2101–2119, https://doi.org/10.1175/JTECH-D-19-0108.1.

——, ——, and ——, 2021: Relative dispersion on the inner shelf: Evidence of a Batchelor regime. *J. Phys. Oceanogr.*, **51**, 519–536, https://doi.org/10.1175/JPO-D-20-0170.1.

Suanda, S. H., and F. Feddersen, 2015: A self-similar scaling for cross-shelf exchange driven by transient rip currents. *Geophys. Res. Lett.*, **42**, 5427–5434, https://doi.org/10.1002/2015GL063944.

——, and Coauthors, 2016: Wind relaxation and a coastal buoyant plume north of Pt. Conception, CA: Observations, simulations, and scalings. *J. Geophys. Res. Oceans*, **121**, 7455–7475, https://doi.org/10.1002/2016JC011919.

——, F. Feddersen, and N. Kumar, 2017: The effect of barotropic and baroclinic tides on coastal stratification and mixing. *J. Geophys. Res. Oceans*, **122**, 10 156–10 173, https://doi.org/10.1002/2017JC013379.

——, ——, M. S. Spydell, and N. Kumar, 2018: The effect of barotropic and baroclinic tides on three-dimensional coastal dispersion. *Geophys. Res. Lett.*, **45**, 11 235–11 246, https://doi.org/10.1029/2018GL079884.

Sutherland, D. A., P. MacCready, N. S. Banas, and L. F. Smedstad, 2011: A model study of the Salish Sea estuarine circulation. *J. Phys. Oceanogr.*, **41**, 1125–1143, https://doi.org/10.1175/2011JPO4540.1.

Thomas, J., J. Lerczak, and J. Moum, 2016: Horizontal variability of high-frequency nonlinear internal waves in Massachusetts Bay detected by an array of seafloor pressure sensors. *J. Geophys. Res. Oceans*, **121**, 5587–5607, https://doi.org/10.1002/2016JC011866.

Thomson, J., 2012: Wave breaking dissipation observed with "SWIFT" drifters. *J. Atmos. Oceanic Technol.*, **29**, 1866–1882, https://doi.org/10.1175/JTECH-D-12-00018.1.

Veneziani, M., C. Edwards, J. Doyle, and D. Foley, 2009: A central California coastal ocean modeling study: 1. Forward model and the influence of realistic versus climatological forcing. *J. Geophys. Res.*, **114**, C04015, https://doi.org/10.1029/2008JC004774.

Walter, R. K., C. B. Woodson, P. R. Leary, and S. G. Monismith, 2014: Connecting wind-driven upwelling and offshore stratification to nearshore internal bores and oxygen variability. *J. Geophys. Res. Oceans*, **119**, 3517–3534, https://doi.org/10.1002/2014JC009998.

——, E. C. Reid, K. A. Davis, K. J. Armenta, K. Merhoff, and N. J. Nidzieko, 2017: Local diurnal wind-driven variability and upwelling in a small coastal embayment. *J. Geophys. Res. Oceans*, **122**, 955–972, https://doi.org/10.1002/2016JC012466.

Warner, J. C., B. Armstrong, R. He, and J. B. Zambon, 2010: Development of a Coupled Ocean–Atmosphere–Wave–Sediment Transport (COAWST) Modeling System. *Ocean Modell.*, **35**, 230–244, https://doi.org/10.1016/j.ocemod.2010.07.010.

Warner, S. J., P. MacCready, J. N. Moum, and J. D. Nash, 2013: Measurement of tidal form drag using seafloor pressure sensors. *J. Phys. Oceanogr.*, **43**, 1150–1172, https://doi.org/10.1175/JPO-D-12-0163.1.

Washburn, L., and E. McPhee-Shaw, 2013: Coastal transport processes affecting inner-shelf ecosystems in the California Current System. *Oceanography*, **26** (3), 34–43, https://doi.org/10.5670/oceanog.2013.43.

——, M. R. Fewings, C. Melton, and C. Gotschalk, 2011: The propagating response of coastal circulation due to wind relaxations along the central California coast. *J. Geophys. Res.*, **116**, C12028, https://doi.org/10.1029/2011JC007502.

Weisberg, R. H., Z. Li, and F. Muller-Karger, 2001: West Florida shelf response to local wind forcing: April 1998. *J. Geophys. Res.*, **106**, 31 239–31 262, https://doi.org/10.1029/2000JC000529.

——, Y. Liu, and D. A. Mayer, 2009: West Florida shelf mean circulation observed with long-term moorings. *Geophys. Res. Lett.*, **36**, L19610, https://doi.org/10.1029/2009GL040028.

White, B. L., and K. R. Helfrich, 2013: Rapid gravitational adjustment of horizontal shear flows. *J. Fluid Mech.*, **721**, 86–117, https://doi.org/10.1017/jfm.2013.41.

Winant, C. D., 1974: Internal surges in coastal waters. *J. Geophys. Res.*, **79**, 4523–4526, https://doi.org/10.1029/JC079i030p04523.

——, E. P. Dever, and M. Hendershott, 2003: Characteristic patterns of shelf circulation at the boundary between central and Southern California. *J. Geophys. Res.*, **108**, 3021, https://doi.org/10.1029/2001JC001302.

Woodson, C., 2018: The fate and impact of internal waves in nearshore ecosystems. *Annu. Rev. Mar. Sci.*, **10**, 421–441, https://doi.org/10.1146/annurev-marine-121916-063619.

——, L. Washburn, J. A. Barth, D. Hoover, A. Kirincich, M. McManus, J. Ryan, and J. Tyburczy, 2009: Northern Monterey Bay upwelling shadow front: Observations of a coastally and surface-trapped buoyant plume. *J. Geophys. Res.*, **114**, C12013, https://doi.org/10.1029/2009JC005623.

Wu, X., F. Feddersen, S. N. Giddings, N. Kumar, and G. Gopalakrishnan, 2020: Mechanisms of mid- to outer-shelf transport of shoreline released tracers. *J. Phys. Oceanogr.*, **50**, 1813–1837, https://doi.org/10.1175/JPO-D-19-0225.1.